

ORBITAL EVOLUTION, ACTIVITY, AND MASS LOSS OF COMET C/1995 O1 (HALE-BOPP).
 II. NUCLEUS AND COMPANIONS AS COMPACT CLUSTERS OF MASSIVE FRAGMENTS

ZDENEK SEKANINA

Jet Propulsion Laboratory, California Institute of Technology, 4800 Oak Grove Drive, Pasadena, CA 91109, U.S.A.

Version June 22, 2021

ABSTRACT

The prime objective is to settle a contradiction between a high nongravitational acceleration affecting the orbital motion of comet C/1995 O1 and its enormous nucleus by modeling it as a *compact cluster of boulder-sized fragments* held together by its own gravity. The nongravitational effect is interpreted as a perturbation of the cluster’s principal, most massive fragment. This and other constraints suggest that the principal fragment was probably 8–9 km across and the entire cluster ~ 150 times less massive than a single-body nucleus of an equal cross-sectional area derived from the Herschel far-infrared photometry of the inactive comet detected near 30 AU from the Sun. The cross-sectional area required the smallest fragments to be a few tens of meters across under a steady-state size distribution. The cluster was at most ~ 200 km in diameter, subject to frequent collisions and significant perturbations by the Sun near perihelion, and apparently a product of tidal fragmentation of the original nucleus, more than 20 km across, at the time of close encounter with Jupiter 4 millennia ago, if the comet’s tensile strength was then as low as several Pa. Published for the first time are the results of a search for companion nuclei in three post-perihelion images taken with the HST’s STIS instrument in 1997–1998. At least 29 such objects < 1200 km (projected) from the primary were detected, with their signals from 2.3% to 25% of the primary’s and the signal-to-noise ratios between 5:1 and 29:1, apparently also cluster-like in nature.

Subject headings: comets: individual (C/1995 O1) — methods: data analysis

1. INTRODUCTION

In Part I (Sekanina & Kracht 2017; hereafter Paper 1) the orbit of comet C/1995 O1 was determined from astrometric observations covering an arc of 17.6 yr; the conditions were examined that existed at the time of a predicted close encounter with Jupiter on –2251 November 7; a correlation was established between a nongravitational acceleration in the comet’s orbital motion and the mass loss rates of water and other ices sublimated from the nucleus; and the production and dynamics of dust ejecta were addressed. Emphasized was the role of non-water compounds — low-volatility organic molecules in particular — in the process of outgassing and their contribution to the total outgassed mass, and also noted was a high mass loading of the gas flow from the nucleus by the released dust. Finally, the issue was brought up of a major disparity between the comet’s mass determined dynamically vs photometrically, which is critical for a makeup of the nucleus, the objective of this study.

2. NONGRAVITATIONAL EFFECT ON THE NUCLEUS AND CONSERVATION-OF-MOMENTUM LAW

It was briefly remarked in Paper 1 that the magnitude of the nongravitational acceleration in the motion of C/1995 O1 was equivalent, after integrating over the orbital period, to a momentum change per unit mass of $2.46 \pm 0.14 \text{ m s}^{-1}$. This result was derived by optimizing a modified version of Marsden et al.’s (1973) nongravitational law, whose scaling distance of 15.36 AU was determined, by fitting 1950 astrometric observations from 1993–2010, as part of a preferred orbital solution. Fully 80% of the effect was contributed by the component of the nongravitational acceleration that was directed away

from the Sun and long recognized as the primary trigger of the outgassing-driven recoil motion of the nucleus, invoked by a conservation-of-momentum law (e.g., Bessel 1836; Whipple 1950; Marsden 1968, 1969).

For a given position in a comet’s orbit, at time t , the conservation-of-momentum law is commonly written as a one-dimensional condition. If only a single species sublimates, the condition reads

$$\mathcal{M} \zeta_{\text{ng}}(t) + \alpha_{\text{gas}}(t) \dot{m}_{\text{sub}}(t) v_{\text{sub}}(t) = 0, \quad (1)$$

where \mathcal{M} is the nucleus’ mass and, at time t , $\zeta_{\text{ng}}(t) > 0$ the nongravitational acceleration, $\dot{m}_{\text{sub}}(t) < 0$ the mass-loss rate by outgassing (i.e., the mass production rate of gas), v_{sub} the velocity with which the gas sublimates, and $\alpha_{\text{gas}}(t) < 1$ a recoil parameter that accounts for a vectorial distribution of the outgassed mass, whereby only a fraction of the momentum generated by the sublimating ice is, in general, transformed into the detected nongravitational acceleration. The recoil parameter depends on the surface distribution of the ice, the nucleus’ shape and rotation, the gas-flow collimation, etc. When a number of different species, n_{gas} , sublimate at the same time, the second term in Equation (1) is to be replaced with a sum $\sum_{i=1}^{n_{\text{gas}}} \alpha_{\text{gas},i} \dot{m}_{\text{sub},i} v_{\text{sub},i}$. Because $v_{\text{sub},i}$ is a function of the mass loading of the gas flow by dust, it could depend not only on $\dot{m}_{\text{sub},i}$, but on $\dot{m}_{\text{sub},j}$ ($j = 1, \dots, n_{\text{gas}}, j \neq i$) as well. The mass of the nucleus is assumed not to vary with time in Equation (1), because $\dot{m}_{\text{sub}} dt \ll \mathcal{M}$.

The conservation-of-momentum condition may also be integrated over the entire orbit, specifically,

$$\mathcal{M} \int_{t_{\pi-\frac{1}{2}P}}^{t_{\pi+\frac{1}{2}P}} \zeta_{\text{ng}}(t) dt + \langle \alpha_{\text{gas}} v_{\text{sub}} \rangle \sum_{i=1}^{n_{\text{gas}}} \int_{t_{\pi-\frac{1}{2}P}}^{t_{\pi+\frac{1}{2}P}} \dot{m}_{\text{sub},i}(t) dt = 0, \quad (2)$$

where t_π is the perihelion time, P the orbital period, and $\langle \alpha_{\text{gas}} v_{\text{sub}} \rangle$ is an orbit-averaged value of the product of the recoil parameter α_{gas} and the sublimation velocity v_{sub} . While the integrated expressions were determined in Paper 1, the product $\langle \alpha_{\text{gas}} v_{\text{sub}} \rangle$ is subject to some uncertainty, but can be constrained as follows.

For any particular ice, the initial velocity of sublimation is subsonic in the presence of dust (Probstein 1969). Hence, if v_{son} is the speed of sound in the gas flow, then

$$v_{\text{sub}}(t) = \beta_{\text{gas}}(t) v_{\text{son}}(t) = \beta_{\text{gas}}(t) \sqrt{\frac{\Re \gamma_{\text{gas}} T_{\text{sub}}(t)}{\mu_{\text{gas}}}}, \quad (3)$$

where $\beta_{\text{gas}} < 1$ depends on the mass loading of the gas flow by dust, \Re is the gas constant ($8.31 \text{ J K}^{-1} \text{ mol}^{-1}$) and T_{sub} , γ_{gas} , and μ_{gas} are, respectively, the gas temperature at sublimation, the heat-capacity ratio, and the molar mass of the species. Because of a rapid drop in the mass-loss rate with heliocentric distance, the greatest weight in the expression for $\langle \alpha_{\text{gas}} v_{\text{sub}} \rangle$ have the values near perihelion. For water, $\gamma_{\text{H}_2\text{O}} = 1.33$, $\mu_{\text{H}_2\text{O}} = 18.02 \text{ g mol}^{-1}$, and for C/1995 O1 at perihelion — employing an isothermal model of Paper 1 — a sonic flow (Mach number of $M = 1$) has a sublimation temperature of $T_{\text{sub,H}_2\text{O}} = 176 \text{ K}$ and, accordingly, $v_{\text{son,H}_2\text{O}} \simeq 330 \text{ m s}^{-1}$.

For carbon monoxide the problem is more complex because of a possible effect of superheating (Fulle et al. 1998). While from the isothermal model one finds that at perihelion $v_{\text{son,CO}} \simeq 130 \text{ K}$, Biver et al.'s (2002) monitoring program of the CO kinetic temperature in C/1995 O1 between perihelion and some 6–8 AU both before and after perihelion suggests $T_{\text{kin,CO}} = 113 \pm 6 \text{ K}$ at perihelion. Since $T_{\text{kin}} > T_{\text{sub}}$, this implies that $v_{\text{son,CO}} < 220 \text{ m s}^{-1}$.

For other ices the isothermal model offers for the speed of sound numbers that are intermediate between carbon monoxide and water. In particular, for complex organic molecules appropriate estimates¹ are $T_{\text{sub}} \simeq 270\text{--}280 \text{ K}$, $\mu_{\text{gas}} \simeq 70 \text{ g mol}^{-1}$, and $\gamma_{\text{gas}} \simeq 1.1$, thus $v_{\text{son}} \simeq 190 \text{ m s}^{-1}$.

For the speed of sound I now accept a representative value of $\langle v_{\text{son}} \rangle = 270 \text{ m s}^{-1}$, a compromise between water and the other parent molecules. With two basic quantities that enter Equation (2) — the integrated nongravitational effect,

$$\Delta V_{\text{ng}} = \int_{t_\pi - \frac{1}{2}P}^{t_\pi + \frac{1}{2}P} \zeta_{\text{ng}}(t) dt = 2.46 \pm 0.14 \text{ m s}^{-1}, \quad (4)$$

and the integrated mass loss of water ice,

$$\Delta \mathcal{M}_{\text{H}_2\text{O}} = \int_{t_\pi - \frac{1}{2}P}^{t_\pi + \frac{1}{2}P} \dot{m}_{\text{sub,H}_2\text{O}}(t) dt = -3.4 \times 10^{15} \text{ g} \quad (5)$$

— already determined in Paper 1, I next turn to a total orbit-integrated mass loss by outgassing. Examination of the contributions from a large set of non-water species resulted in Paper 1 in a total *documented* mass loss of 175% of the loss of water and a *predicted* range of total losses well over 200%, a conclusion based primarily on a recognition of an apparently highly incomplete inventory of

complex organic molecules. Crovisier et al. (2004) similarly argued that there were still many molecular species to be discovered in comets. However, rather than the orbit-integrated mass-loss data they used near-perihelion abundances, in which case the degree of incompleteness — while still detectable — appears to be less prominent. Based on the results of Paper 1, I adopt for the total orbit-integrated mass loss by outgassing a representative value of 250% of the mass loss by water ice:

$$\begin{aligned} \Delta \mathcal{M}_{\text{gas}} &= \sum_{i=1}^{n_{\text{gas}}} \int_{t_\pi - \frac{1}{2}P}^{t_\pi + \frac{1}{2}P} \dot{m}_{\text{sub},i}(t) dt \\ &= 2.5 \Delta \mathcal{M}_{\text{H}_2\text{O}} = -8.5 \times 10^{15} \text{ g}. \end{aligned} \quad (6)$$

Equation (2), in which — following (3) — $\langle \alpha_{\text{gas}} v_{\text{sub}} \rangle$ is replaced with $\langle \alpha_{\text{gas}} \beta_{\text{gas}} v_{\text{son}} \rangle$, can be used to estimate an upper limit on the mass of the nucleus by substituting $\langle v_{\text{son}} \rangle$ for this expression:

$$\mathcal{M} = \langle \alpha_{\text{gas}} \beta_{\text{gas}} v_{\text{son}} \rangle \frac{|\Delta \mathcal{M}_{\text{gas}}|}{\Delta V_{\text{ng}}} < \langle v_{\text{son}} \rangle \frac{|\Delta \mathcal{M}_{\text{gas}}|}{\Delta V_{\text{ng}}}. \quad (7)$$

The inequality follows from α_{gas} and β_{gas} being always smaller than unity. This relation indicates that since the sublimation velocity amounted to less than the speed of sound and the gas flow was imperfectly collimated, the momentum of the outgassed mass per orbit should have been less than $2.3 \times 10^{20} \text{ g cm s}^{-1}$ and the nucleus less than $1 \times 10^{18} \text{ g}$ in mass. Assuming a bulk density of 0.4 g cm^{-3} , the diameter should under no circumstances have exceeded 17 km. In reality, the heavy mass loading of the gas flow by dust, which — based on the results of Paper 1 *and* including the contributions from as yet undetected molecules, as implied by Equation (6) — is likely to have exceeded 4, suggests an initial Mach number of $M < 0.3$ for the gas (Probstein 1969), while the absence of perfect gas-flow collimation may have reduced effects of the momentum by another factor of 1.5 or more. And even though there may have existed phenomena that worked in the opposite direction (such as recondensation; fallback on the surface by boulders; etc.), the momentum imparted to the nucleus should still have been substantially lower than implied by $\langle v_{\text{son}} \rangle$. Allowing the product of $\langle \alpha_{\text{gas}} \beta_{\text{gas}} \rangle$ to vary from 0.1 to a stretched value of 0.35, the diameter of a model spherical nucleus consistent with Equation (7) should be in a range from $\sim 8 \text{ km}$ to $\sim 12 \text{ km}$.

Szabó et al. (2011, 2012) analyzed several images of C/1995 O1 along the post-perihelion leg of the orbit up to a heliocentric distance of 32 AU. The authors concluded that the comet's activity ceased between late 2007 and early 2009; this estimate can be refined with use of the results by Kramer et al. (2014), who still detected minor activity in 2008 August–September. The inactive nucleus was detected at optical wavelengths of $0.55\text{--}0.9 \mu\text{m}$ on a few occasions, including with the Hubble Space Telescope (HST) on 2009 September 8 and with the Very Large Telescope (VLT) on 2011 October 5–25. It was also observed with the Herschel Space Observatory at $70 \mu\text{m}$ on 2010 June 10. These observations allowed Szabó et al. (2012) to determine separately a cross-sectional area of the nucleus, yielding a mean diameter of $74 \pm 6 \text{ km}$ with an axial ratio of at least 1.72 ± 0.07 ; and a post-perihelion geometric albedo of 0.081 ± 0.009 , in contrast to a preperihelion albedo of only 0.03 ± 0.01 .

¹ Statistically, numerous hydrocarbons appear to satisfy a relation between the molar mass (in g mol^{-1}) and the heat-capacity ratio that is approximately expressed as $\gamma_{\text{gas}} = 1.56 - 0.25 \log \mu_{\text{gas}}$ for $30 < \mu_{\text{gas}} < 120 \text{ g mol}^{-1}$.

Szabó et al.’s (2012) determination of the nucleus’ dimensions is in remarkably good agreement with an earlier result by Sekanina (1999a), who derived an average diameter of 71 ± 4 km (cf. Table 5) from six HST images exposed between October 1995 and October 1996 (i.e., long before perihelion). Other researchers arrived at less consistent dimensions, commenting on large discrepancies among the determinations by diverse methods. Employing the same HST images but a different approach, Weaver & Lamy (1999) did estimate the most probable diameter at 70 km, yet not entirely ruling out 30–40 km; they also reviewed the results by another group of an occultation of a star by the comet and arrived at an admittedly model dependent diameter of less than 52 km, while from three independent microwave observations the diameter came out to be near 40 km. Thermal-infrared observations aboard the Infrared Space Observatory resulted in a diameter of 70–112 km depending on the applied physical model (Jorda et al. 2000). Re-reviewing the constraints from these data and near-perihelion radiometric data, Fernández (2002) estimated the diameter at 60 ± 20 km. In their summary table, Lamy et al. (2004) provide two numbers for the nucleus’ diameter, 74 km and 60 km, with no errors provided.

In summary, the *dimensions of an inactive nucleus of C/1995 O1* derived for a single-body model from a far-infrared observation at a record large heliocentric distance do *under no circumstances accommodate the magnitude of the outgassing-driven nongravitational acceleration* in the comet’s motion. In the conservation-of-momentum equation, this disparity exceeds two orders of magnitude in terms of the mass of the nucleus, so that one confronts a *major contradiction*. Interestingly, this problem was independently mentioned by Sosa & Fernández (2011), yet it has never been solved nor its possible implications seriously addressed in the literature.

3. NUCLEUS OF C/1995 O1 AS A COMPACT CLUSTER OF FRAGMENTS OF THE ORIGINAL BODY

I argue that the only feasible solution to this contention requires one to postulate that the nucleus of C/1995 O1 at its recent return to perihelion was being made up of a *compact cluster of massive fragments* into which the original nucleus broke up by the action of tidal forces exerted by Jupiter in the course of the comet’s close encounter with the planet in the 3rd millennium BCE (Paper 1).

I further postulate that the detected nongravitational acceleration refers to the principal, most massive fragment, 8–12 km in diameter and orbiting the Sun close to the cluster’s center of mass, while the nongravitational accelerations on other outgassing fragments trigger minor perturbations of their motions relative to the principal fragment and remain undetected.

For this model to be physically meaningful, the cluster must be bound enough by gravity to survive as a densely-packed assemblage over more than 4000 yr against both the Sun’s perturbations and collisional self-destruction. It is also necessary to account for the observed nucleus’ brightness in terms of a cross-sectional area of the (optically thin) cloud of fragments, to establish their size range and distribution to make the model self-consistent, and to describe the fragment properties in the context of both observations and constraints on the model — including its gravitational stability and collisional history.

4. STABILITY OF GRAVITATIONALLY BOUND ORBITS: THE ANALOGS

Globular clusters come to mind as a convenient cosmic analog for investigating the conditions of gravity-driven stability of a compact cometary assemblage. Kennedy’s (2014) recent paper extensively deals with this issue and predicts the radius of stability, r_{st} , employing Mardling’s (2008) analysis. The outcome is a simple expression

$$r_{\text{st}} = r_{\text{gal}} f_0 \left(\frac{\mathcal{M}_{\text{gc}}}{\mathcal{M}_{\text{gal}}} \right)^{\frac{1}{3}}, \quad (8)$$

where \mathcal{M}_{gal} , \mathcal{M}_{gc} , r_{gal} , and f_0 are, respectively, the mass of the galaxy, the mass of the globular cluster, the distance of its closest approach to the center of the galaxy, and a parameter that is a function of the globular cluster’s orbital eccentricity. In a limiting parabolic scenario, the orbits of all stars in the cluster are stable when $f_0 < 0.18$. For comparison, the radius of Hill’s sphere of C/1995 O1 at time t is (e.g., Chebotarev 1964)

$$r_{\text{Hill}}(t) = r_{\text{st}}(t, h_0) = r(t) h_0 \left(\frac{\mathcal{M}_{\text{C}}}{\mathcal{M}_{\text{Sun}}} \right)^{\frac{1}{3}}, \quad (9)$$

where $h_0 = 3^{-\frac{1}{3}} = 0.69$ and \mathcal{M}_{Sun} , $\mathcal{M}_{\text{C}}(t)$, and $r(t)$ are, respectively, the mass of the Sun, and the comet’s mass and heliocentric distance at time t . Kennedy’s (2014) results show that the stability-zone’s radius is about four or more times smaller than the radius of Hill’s sphere.

Two papers by Hamilton & Burns (1991, 1992) on orbital stability zones about asteroids are highly relevant. The authors fortunately extended the range of investigated orbital eccentricities to 0.9, thereby covering effectively comets as well. Establishing the stability of gravitationally bound orbits of particles around asteroids as a function of a deviation from orbit circularity, they also considered effects of the Coriolis force, orbital inclination, and solar radiation pressure. They further showed that escape to interplanetary space was not the only loss mechanism for particles in the initially bound trajectories; impact on the asteroid’s surface was another means of removal. Their effort focused on the determination of a ratio equivalent to $D_{\text{st}}/D_{\text{C}}$, where D_{st} is the stability-zone’s diameter (equaling $2r_{\text{st}}$) and D_{C} is the comet’s or asteroid’s diameter. For elongated orbits they independently concluded that the heliocentric distance in Equation (9) was to be taken at perihelion, $r(t_{\pi}) = q$, so that

$$\frac{D_{\text{st}}}{D_{\text{C}}} = 191.76 h_0 q \rho^{\frac{1}{3}}, \quad (10)$$

where ρ is the bulk density of the comet’s nucleus or the asteroid in g cm^{-3} and q is in AU.

Hamilton & Burns (1991) demonstrated that the loss of orbital stability was considerably higher among particles in prograde than in retrograde trajectories. In fact, extrapolation to the parent body’s parabolic orbit would leave practically no gravitationally bound particles after 20 yr, the period of time over which their integrations extended. For retrograde orbits, impacts on the asteroid’s surface became extremely rare and extrapolation of the stability-zone’s radius to parabolic motion was uncertain, in part because of insufficient integration times, but some particles were likely to have survived in bound orbits.

Estimating crudely from Hamilton & Burns' plot that $D_{\text{st}}/D_{\text{C}} > 10$, one obtains $h_0 > 0.08$ from Equation (10) with $\rho = 0.4 \text{ g cm}^{-3}$. Combining this lower limit with the upper bound implied by Kennedy's (2014) computations, I adopt in the following $h_0 = 0.1$ to derive D_{st} for C/1995 O1.

Hamilton & Burns (1992) found that radiation pressure eliminated from the stable orbits all particles smaller than $\sim 1 \text{ mm}$ for an asteroid $\sim 200 \text{ km}$ in diameter and all particles smaller than $\sim 1 \text{ cm}$ for an asteroid $\sim 20 \text{ km}$ in diameter. There was little difference between radiation-pressure effects on prograde and retrograde orbits. Based on these results, it can be expected that no fragments smaller than a few centimeters would survive in stable orbits in the presumed nucleus' cluster of C/1995 O1.

The results by Hamilton & Burns (and others referred to in their papers) were a product of solving a three-body problem: the Sun, an asteroid, and a single orbiting particle. By contrast, a cluster of fragments involves of course an n -body problem, as described below.

5. FORMULATION OF A COMPACT CLUSTER MODEL

To describe the compact cluster of fragments, it is desirable to first constrain its properties by requiring that they satisfy relevant observations. If a product of a collisional process that began with an initial tidal breakup in close proximity of Jupiter and was characterized by very low relative velocities (Section 8), one expects the differential size distribution function of fragments, i.e., their number, $d\mathcal{N}_{\text{frg}}$, with diameters from D to $D+dD$, to eventually approach steady state. At a constant bulk density, this scenario implies (Dohnanyi 1969; Williams & Wetherill 1994)

$$d\mathcal{N}_{\text{frg}}(D) = k_{\text{frg}} D^{-\frac{7}{2}} dD, \quad (11)$$

where k_{frg} is a normalization constant. The cumulative distribution, i.e., the number of fragments whose diameters are greater than, or equal to, D , is then

$$\mathcal{N}_{\text{frg}}(D) = \int_D^\infty k_{\text{frg}} D^{-\frac{7}{2}} dD = \frac{2k_{\text{frg}}}{5} D^{-\frac{5}{2}}. \quad (12)$$

For the principal fragment, whose diameter D_0 was constrained by the orbital-momentum condition (Sections 2 and 3) to a range of 8–12 km, this expression requires that $\mathcal{N}_{\text{frg}}(D_0) = 1$, so that $k_{\text{frg}} = \frac{5}{2} D_0^{5/2}$ and Equation (12) simplifies to

$$\mathcal{N}_{\text{frg}}(D) = \left(\frac{D_0}{D}\right)^{\frac{5}{2}}. \quad (13)$$

If, reckoned in the order of decreasing size, an i -th fragment ($\mathcal{N}_{\text{frg}} = i$) has a diameter D_{i-1} , the diameter D_i of the next smaller, $(i+1)$ st fragment equals

$$D_i = D_{i-1} \left[1 + \frac{1}{\mathcal{N}_{\text{frg}}(D_{i-1})}\right]^{-\frac{2}{5}} = D_{i-1} \left(\frac{i}{i+1}\right)^{\frac{2}{5}}. \quad (14)$$

For example, the diameter of the second largest fragment is expected to be $0.76 D_0$, its mass should be 0.435 the mass of the principal fragment, and, if outgassing, its nongravitational acceleration should amount to 1.32 the acceleration of the principal fragment. An expression similar to Equation (14) can be derived for D_i as a function of D_{i+1} and $\mathcal{N}_{\text{frg}}(D_{i+1})$.

The cross-sectional area of the nucleus' model by Szabó et al. (2012), $X_{\text{Sz}} = 4300 \text{ km}^2$, is now to be interpreted as a sum of the cross-sectional areas of all surviving fragments in the cluster that is presumed to be optically thin, $X_{\text{frg}} = X_{\text{Sz}}$; it serves as another constraint on the distribution function,

$$X_{\text{frg}} = \frac{5}{2} D_0^{\frac{5}{2}} \int_{D_\star}^{D_0} \frac{1}{4} \pi D^2 \cdot D^{-\frac{7}{2}} dD = \frac{5}{4} \pi D_0^2 \left(\sqrt{\frac{D_0}{D_\star}} - 1\right), \quad (15)$$

where D_\star is the diameter of the smallest fragment that contributes to the observed cross-sectional area X_{frg} . As it follows from Equation (15) that

$$D_\star = D_0 \left(1 + \frac{4X_{\text{frg}}}{5\pi D_0^2}\right)^{-2}, \quad (16)$$

the total number of fragments in the cluster is equal to

$$\mathcal{N}_{\text{frg}}^\star = \mathcal{N}_{\text{frg}}(D_\star) = \left(\frac{D_0}{D_\star}\right)^{\frac{5}{2}} = \left(1 + \frac{4X_{\text{frg}}}{5\pi D_0^2}\right)^5 \quad (17)$$

and an average fragment diameter in the distribution is

$$\langle D \rangle = \frac{\int_{D_\star}^{D_0} D \cdot D^{-\frac{7}{2}} dD}{\int_{D_\star}^{D_0} D^{-\frac{7}{2}} dD} = \frac{5}{3} D_\star \left[1 - \left(\frac{D_\star}{D_0}\right)^{\frac{3}{2}}\right] \cdot \left[1 - \left(\frac{D_\star}{D_0}\right)^{\frac{5}{2}}\right]^{-1}. \quad (18)$$

The mass contained in the cluster of fragments equals

$$\begin{aligned} \mathcal{M}_{\text{frg}} &= \frac{5}{2} D_0^{\frac{5}{2}} \int_{D_\star}^{D_0} \frac{1}{6} \pi \rho D^3 \cdot D^{-\frac{7}{2}} dD \\ &= \frac{5\pi}{6} \rho D_0^3 \left(1 - \sqrt{\frac{D_\star}{D_0}}\right) = 5\mathcal{M}_0 \left[1 - (\mathcal{N}_{\text{frg}}^\star)^{-\frac{1}{5}}\right], \end{aligned} \quad (19)$$

where ρ is a bulk density of the fragments and \mathcal{M}_0 the mass of the principal fragment, $\mathcal{M}_0 = \frac{1}{6} \pi \rho D_0^3$, which always exceeds 20% of the cluster's total mass. The minimum and average fragment diameters, the number of fragments, and the cluster's total mass, all derived from the observed cross-sectional area, are for three principal fragment's diameters from the adopted range (Section 3) listed in the top section of Table 1.

6. BIRTH AND EARLY EVOLUTION OF COMPACT CLUSTER

The postulation of a breakup of the original nucleus of C/1995 O1 that was triggered by Jupiter's tidal forces at or very near the time of closest approach to the planet in November of -2251 (Section 1) is a plausible hypothesis for the origin of the compact cluster, because if it had come into existence way before the encounter, Jupiter's gravity field would have dissipated the cluster into a long filament of fragments at the time of the event.

As described in detail in Paper 1, the comet has not approached Jupiter to within 0.7 AU since the encounter, but it passed through perihelion about 13 months after the near miss, at a heliocentric distance almost identical to that in 1997. During the more than 42 centuries the size distribution of fragments, especially near its lower end should have changed dramatically, as illustrated by

Hamilton & Burns (1992) for asteroids. All fragments smaller than a few centimeters across were removed by radiation pressure within years after the breakup. Of the remaining fragments, including the more sizable ones, all those moving in prograde orbits were soon lost as well.² For fragments in retrograde orbits the situation is less clear, but, as a rule of thumb, one can assume that at least 50% of them failed to survive until the 1997 apparition. Because the initial orbital velocities of fragments relative to the cluster's center of mass (dictated by the rotation of the original nucleus at the time of breakup) were very low, the high collisional rate (Section 8) must have soon brought a near equilibrium between the numbers of fragments moving in prograde and retrograde orbits, so for the sake of argument one can assume that about one quarter of all fragments with diameters larger than D_\star survived until the 1997 apparition.

If no fragment with a diameter smaller than D_\star but one quarter of the fragments with diameters $D_\star \leq D \leq D_0$ survived to the 1997 apparition, the mass \mathcal{M}_C of the original nucleus of C/1995 O1 at the time of encounter with Jupiter is estimated to have equaled

$$\mathcal{M}_C = \mathcal{M}_C \sqrt{D_\star/D_0} + 4\mathcal{M}_{\text{frag}}, \quad (20)$$

where the mass $\mathcal{M}_{\text{frag}}$ is given by Equation (19). Solving Equation (20) for \mathcal{M}_C , one finds in terms of the principal fragment's parameters:

$$\mathcal{M}_C = \frac{10\pi}{3} \rho D_0^3 = 20\mathcal{M}_0. \quad (21)$$

This is of course a very crude estimate, but it is needed only for an assessment of the probability of tidal breakup in Section 7. In the range of the three solutions in Table 1, the original nucleus was between 2.1 and 7.3×10^{18} g in mass and between 21 and 33 km in diameter (at the adopted bulk density of 0.4 g cm^{-3}), a considerably less impressive and statistically more probable size than 74 km. Yet, because of the greater mass and the very limited volume of space involved, the collisional rate in the early phase of cluster evolution should have been orders of magnitude higher than at the 1997 apparition.

Judging from the numerical experiments by Hamilton & Burns (1991, 1992), much of the dust generated in the course of fragmentation is expected to have been blown away by solar radiation pressure, especially near the perihelion passage 13 months after the Jovian encounter, whereas smaller, active boulder-sized objects were subjected to nongravitational accelerations whose effects ultimately were not unlike those of radiation pressure. I return to the issue of small fragments in Section 8, after introducing a constraint on the collisional rate.

² Fragments larger than a few centimeters but smaller than D_\star in diameter (Table 1) were probably removed by the outgassing-driven momentum, whose influence — at least at heliocentric distances of up to a few AU — resembles that of solar radiation pressure, varying as an inverse diameter. For example, scaling the observed effect, a fragment 50 m in diameter is expected at 1 AU from the Sun to be subjected to an outgassing-driven acceleration on the order of 0.002 the Sun's gravitational acceleration, equivalent to a radiation-pressure acceleration on a particle of about 1.5 mm in diameter at the same density. As activity ceases at larger heliocentric distances, so does the momentum and, accordingly, the resulting orbit-integrated effect is more heavily dependent on its magnitude near the Sun than is radiation pressure.

7. TIDAL FORCE OF JUPITER VS DIMENSIONS AND TENSILE STRENGTH OF ORIGINAL NUCLEUS

Consider the original, pre-encounter nucleus of comet C/1995 O1 as a porous rigid rotating spherical aggregate of dust and ices in static equilibrium, moving in a strongly hyperbolic orbit about Jupiter and exposed to its tidal forces. A comprehensive stress theory by Aggarwal & Oberbeck (1974) suggests that at a Jovicentric distance Δ_J fissures should start propagating from the equatorial regions on the nucleus' surface at which Jupiter is rising above, or setting below, the local horizon, when the tensile strength, T_{tens} , satisfies a condition

$$T_{\text{tens}} = \frac{10}{19} P_c \left(\frac{R_J}{\Delta_J} \right)^3 \frac{\rho_J}{\rho}, \quad (22)$$

where R_J and ρ_J are Jupiter's radius and mean density, ρ is again the nucleus' bulk density, and

$$P_c = \frac{1}{6} \pi G \rho^2 D_C^2 \quad (23)$$

is the gravitational pressure in the center of the nucleus of diameter D_C , with G being the gravitational constant. Inserting $\Delta_J/R_J = 10.73$ (Paper 1), $\rho_J = 1.33 \text{ g cm}^{-3}$, and $\rho = 0.4 \text{ g cm}^{-3}$, the tensile strength is between 3.7 Pa and 8.4 Pa for the original nucleus 21.7 km to 32.6 km in diameter (Table 1). These tensile strength values are near the lower end of a range reported by Groussin et al. (2015) [3 Pa] and Basilevsky et al. (2016) [>1.5 Pa] from their studies of outcropped consolidated material in cliff-like features on the nucleus' surface of comet 67P. As a short-period comet, 67P was exposed to processes such as sintering, which have a tendency to increase the strength of material and which C/1995 O1 is not expected to have

Table 1
Nucleus of C/1995 O1 As a Compact Cluster of Fragments^a

Parameter	Adopted Diameter D_0 of Principal Fragment		
	8 km	10 km	12 km
Cluster of Fragments at 1997 Apparition ^{a,b}			
Principal fragment's mass, \mathcal{M}_0 (10^{17} g)	1.07	2.09	3.62
Diameter of smallest fragment, D_\star (m)	24.4	70.0	162
Average fragment diameter, $\langle D \rangle$ (m)	40.7	117	270
Total number of fragments, N_{frag}^* (10^5)	19.5	2.44	0.47
Total mass of fragments, $\mathcal{M}_{\text{frag}}$ (10^{17} g)	5.07	9.60	16.0
Diameter of stability zone ^c , D_{st} (km)	173	214	254
Original Nucleus at Jovian Encounter Time ^{b,d}			
Mass, \mathcal{M}_C (10^{17} g)	21.4	41.8	72.4
Diameter, D_C (km)	21.7	27.1	32.6
Escape velocity at surface, V_{esc} (m s^{-1})	5.13	6.40	7.70
Equatorial rotation velocity, V_{equ} (m s^{-1})	1.67	2.08	2.51
Central gravitational pressure, P_c (Pa)	2633	4106	5942
Tensile strength (upper limit), T_{tens} (Pa)	3.7	5.8	8.4

Notes.

^a Constrained by sum of cross-sectional areas of all fragments equaling $X_{\text{frag}} = 4300 \text{ km}^2$.

^b For bulk density of $\rho = 0.4 \text{ g cm}^{-3}$.

^c At perihelion.

^d For rotation period of 11.35 hr (Licandro et al. 1998) and minimum encounter distance of $\Delta_J = 10.73$ Jupiter's radii (Paper 1).

experienced before the encounter. Its tidal breakup in close proximity of Jupiter should accordingly be judged as plausible.

Once a fissure began to propagate inside the comet's nucleus, a separation of the early fragments was only a matter of time. The fragmentation may have been assisted by the rotational velocity, which — if the spin rate was close to that observed during the 1997 apparition (a rotation period of ~ 11.35 hr; Licandro et al. 1998) — amounted to between 1.7 m s^{-1} and 2.5 m s^{-1} . Since the velocity of escape equaled 5.1 m s^{-1} to 7.7 m s^{-1} , the early fragments moved along ballistic trajectories, resulting in imminent impacts, further fragmentation, and random walk of secondary fragments superposed on their rotationally-driven motions. The momentum should have progressively built up to make the developing cluster of colliding fragments slowly expand around its center of mass. On the assumption that the cluster was gradually acquiring spherical symmetry, a root-mean-squared circular velocity, $\langle V_{\text{circ},\ell}^2 \rangle^{\frac{1}{2}}$, at distances between $\ell - d\ell$ and ℓ should satisfy a condition

$$\langle V_{\text{circ},\ell}^2 \rangle 4\pi\ell^2 d\ell = \frac{GM_f(\ell)}{\ell} 4\pi\ell^2 d\ell, \quad (24)$$

where $\mathcal{M}_f(\ell)$ is the mass of the fragments located at distances smaller than ℓ from the center of mass, to whose gravitational attraction the fragments orbiting between $\ell - d\ell$ and ℓ are subjected to. All fragments at distances greater than ℓ represent minor perturbers. Assuming the cluster's spatial density to be independent of the distance from the center of mass, $\mathcal{M}_f(\ell)$ varies as the volume confined within ℓ , and if D_{frg} is the cluster's diameter, the root-mean-squared circular velocity averaged over the cluster, $\langle V_{\text{circ}}^2 \rangle^{\frac{1}{2}}$, is determined by a condition

$$\langle V_{\text{circ}}^2 \rangle \int_0^{\frac{1}{2}D_{\text{frg}}} \ell^2 d\ell = \int_0^{\frac{1}{2}D_{\text{frg}}} \frac{GM_{\text{frg}}}{\ell} \left(\frac{2\ell}{D_{\text{frg}}} \right)^3 \ell^2 d\ell, \quad (25)$$

from which

$$\langle V_{\text{circ}}^2 \rangle^{\frac{1}{2}} = \left(\frac{6GM_{\text{frg}}}{5D_{\text{frg}}} \right)^{\frac{1}{2}}, \quad (26)$$

where \mathcal{M}_{frg} is given by Equation (19).

8. RATE OF COLLISIONS AMONG FRAGMENTS AND THE CLUSTER'S SIZE

Consider a spherical fragment of a diameter D_i moving with a velocity $V_{i,j}$ relative to another fragment whose diameter is D_j . The cross-sectional area for a collision between these two fragments equals (e.g., Kessler 1981)

$$\sigma_{i,j} = \frac{\pi}{4} (D_i + D_j)^2, \quad (27)$$

where the fragments' escape velocity is being neglected. If ν is a number density of fragments in the cluster, i.e., their number per unit volume, an average number of collisions that the fragment with a diameter D_i experiences per unit time, $\dot{N}_{\text{coll}}^{(i)}$, then equals

$$\dot{N}_{\text{coll}}^{(i)} = \nu \langle \sigma_i \rangle \langle V_{\text{rel},i}^2 \rangle^{\frac{1}{2}}, \quad (28)$$

where $\langle \sigma_i \rangle$ is an average collisional cross-sectional area for a fragment of diameter D_i and $\langle V_{\text{rel},i}^2 \rangle^{\frac{1}{2}}$ is its root-

mean-squared impact velocity averaged over all fragments with which it collides. If the population of fragments has the size distribution introduced in Section 4, the collisional cross-sectional area $\langle \sigma_i \rangle$ equals

$$\begin{aligned} \langle \sigma_i \rangle &= -\frac{5}{2} D_{\star}^{\frac{5}{2}} \left[1 - \left(\frac{D_{\star}}{D_0} \right)^{\frac{5}{2}} \right]^{-1} \int_{D_{\star}}^{D_0} \sigma_{i,j} D_j^{-\frac{7}{2}} dD_j \\ &= \frac{\pi}{4} D_i^2 \left[1 + \frac{5}{\Gamma_5} \frac{D_{\star}}{D_i} \left(\frac{2\Gamma_3}{3} + \frac{D_{\star}}{D_i} \right) \right], \end{aligned} \quad (29)$$

where

$$\Gamma_m = \sum_{k=0}^{m-1} \left(\frac{D_{\star}}{D_0} \right)^{\frac{1}{2}k} = \frac{1 - \sqrt{(D_{\star}/D_0)^m}}{1 - \sqrt{D_{\star}/D_0}}. \quad (30)$$

Averaging now D_i over all fragment diameters between D_{\star} and D_0 , the mean cross-sectional area $\langle \sigma \rangle$ for collisions between any two such fragments becomes

$$\begin{aligned} \langle \sigma \rangle &= -\frac{5}{2} D_{\star}^{\frac{5}{2}} \left[1 - \left(\frac{D_{\star}}{D_0} \right)^{\frac{5}{2}} \right]^{-1} \int_{D_{\star}}^{D_0} \langle \sigma_i \rangle D_i^{-\frac{7}{2}} dD_i \\ &= \frac{5\pi}{2\Gamma_5} D_{\star}^2 \left(1 + \frac{5\Gamma_3}{9\Gamma_5} \right), \end{aligned} \quad (31)$$

and an average number of collisions per unit time, \dot{N}_{coll} , experienced by the fragments with diameters between D_{\star} and D_0 is

$$\dot{N}_{\text{coll}} = \nu \langle \sigma \rangle \langle V_{\text{rel}}^2 \rangle^{\frac{1}{2}}, \quad (32)$$

where $\langle V_{\text{rel}}^2 \rangle^{\frac{1}{2}}$ is their root-mean-squared velocity averaged over the cluster. I now assume that this velocity varies in proportion to the root-mean-squared average circular velocity, derived in Section 5,

$$\langle V_{\text{rel}}^2 \rangle^{\frac{1}{2}} = \eta \langle V_{\text{circ}}^2 \rangle^{\frac{1}{2}}. \quad (33)$$

In his elaborate collisional model for the asteroid population, Dohnanyi (1969) adopted an impact velocity equivalent to $\eta \simeq 0.29$. However, the motions of asteroids in the belt are much more organized than are fragments in the proposed cluster, for which η should be much greater but not exceeding unity, because there is not enough energy in the system to achieve $\langle V_{\text{rel}}^2 \rangle \gg \langle V_{\text{circ}}^2 \rangle$.

An important constraint follows from Schr apler et al.'s (2012) microgravity experiments that showed that in order for fluffy dust aggregates to fragment upon impact, their relative velocity should be at least 0.4 m s^{-1} , since at lower velocities they bounce or stick. Similar independent experiments by Gunkelmann et al. (2016) suggest that for highly porous submicron-grain agglomerates, comparable in porosity to cometary nuclei, the minimum impact velocity triggering fragmentation is still lower, at $\sim 0.17 \text{ m s}^{-1}$. Since the impact velocity is a function of the cluster size, which in turn depends on the velocity, the parameter η is constrained but not well determined.

With the number density of fragments in the cluster being

$$\nu = \frac{6\mathcal{N}_{\text{frg}}^{\star}}{\pi D_{\text{frg}}^3} = \frac{6}{\pi D_{\text{frg}}^3} \left(\frac{D_0}{D_{\star}} \right)^{\frac{5}{2}}, \quad (34)$$

I insert from Equations (31), (33), and (34) as well as from (26), (19), and (15) into Equation (32) and obtain

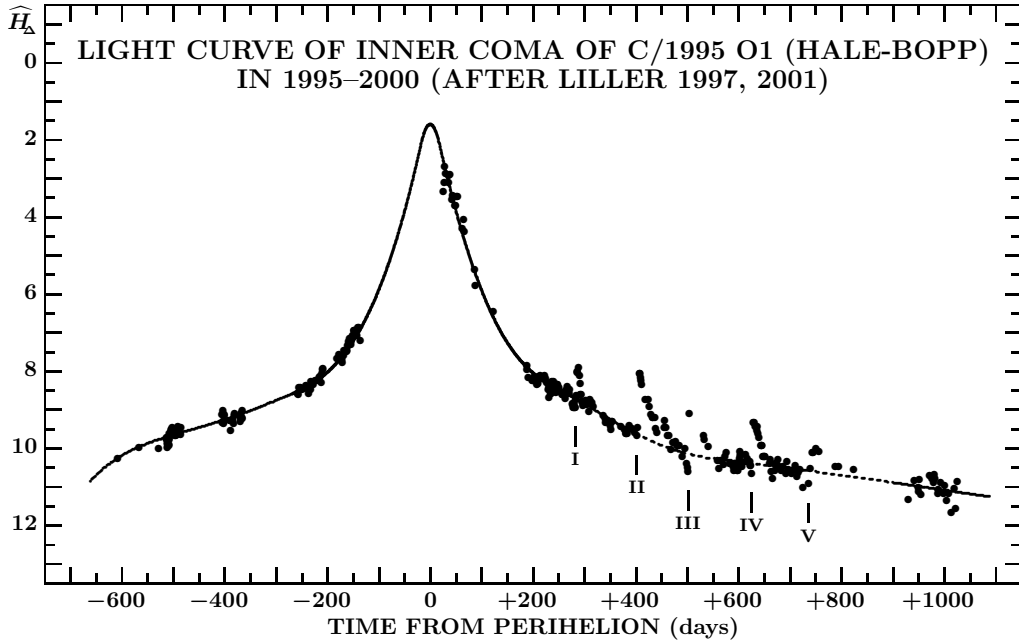


Figure 1. Visual light curve of the inner coma of comet C/1995 O1 (normalized to a nucleus-centered field of 24 660 km on a side when observed from a distance of 1 AU) based on the CCD observations by Liller (1997, 2001) made with a 20-cm f/1.5 Celestron camera between 1995 August 2 and 2000 January 21 (608 days preperihelion to 1025 days post-perihelion). The curve is very smooth before perihelion, but dotted with at least five prominent flare-ups after perihelion, between 1998 January and 1999 April, when the comet was 4 AU to 8.2 AU from the Sun. The onset times of the events are marked I–V. Their amplitudes, 0.7–1.6 mag, imply a sudden increase in the cross-sectional area of the dust ejecta in the 34'' field of up to nearly 3 million km² at an assumed geometric albedo of 0.04 (Table 2).

for a mean free time between two consecutive collisions, $\tau_{\text{coll}} = \dot{N}_{\text{coll}}^{-1}$, an expression

$$\tau_{\text{coll}} = \frac{\sqrt{5}}{30\eta} \frac{\Gamma_5^2}{\Gamma_5 + \frac{5}{9}\Gamma_3^2} (G\rho X_{\text{frg}})^{-\frac{1}{2}} D_{\star}^{\frac{1}{4}} D_0^{-\frac{11}{4}} D_{\text{frg}}^{\frac{7}{2}}. \quad (35)$$

The mean free time depends heavily on the dimensions of the cluster and the principal fragment, but only weakly on the size of the smallest fragment, which besides its quartic root enters the expression via the sums Γ_3 and Γ_5 .

Equation (35) can in principle serve to determine the size of the cluster at the 1997 apparition as a function of D_0 , once the collisional mean free time τ_{coll} and the impact velocity parameter η are known. Although the exact dimensions of the cluster at the 1997 apparition are unknown, they are rather strongly constrained; the cluster's gravitational stability over more than four millennia requires that its diameter not exceed the stability limit at large heliocentric distances, where the comet spends nearly all of its life. Another upper limit is provided by the HST images taken between October 1995 and October 1996; one pixel, which the cluster's diameter should never exceed by more than a factor of about two, equaled between 90 km and 220 km. On the other hand, assuming that the cluster was optically thin, its diameter should much exceed Szabó et al.'s (2012) 74 km.

9. LILLER'S DETECTION OF RECURRING FLARE-UPS AND THEIR PROPOSED INTERPRETATION

A pair of important papers on C/1995 O1 was written by Liller (1997, 2001). He monitored the brightness of the inner coma using a 20-cm f/1.5 Celestron camera, a CCD detector, and a filter to obtain magnitudes in the V system. His dataset consists of exposures on 360 nights,

covering a time period of nearly $4\frac{1}{2}$ yr, from 1995 August 2 (608 days before perihelion) to 2000 January 21 (1025 days after perihelion). The comet was 7.06 AU and 10.28 AU from the Sun on, respectively, the former and the latter dates. For each exposure Liller measured an apparent magnitude \hat{H} in a square field of 34'' on a side, with the nucleus in its center, and converted it to \hat{H}_{Δ} , by removing the effect of a variable field size due to the comet's changing geocentric distance Δ , with an expression $\hat{H}_{\Delta} = \hat{H} - 2.5 \log \Delta$. This light curve is reproduced in Figure 1 as a function of the time from perihelion.

Liller (2001) called attention to a prominent anomaly in the light curve, which is very smooth before perihelion but dotted with at least five flare-ups after perihelion. He noted that the flare-ups were distributed approximately uniformly in time, with gaps of 96 days to 125 days; that the peak amplitudes ranged from 0.7 mag to 1.6 mag; that their heliocentric distances varied from 4.0 AU to 8.1 AU; and that the expansion velocities of the ejected material were confined to a range from 62 m s⁻¹ to 217 m s⁻¹. The peaks of the five flare-ups were observed between 1998 January 11 and 1999 April 14, and there could well have been two additional flare-ups, one in late August 1997 and the other in mid-October 1999. Liller expressed his belief that the flare-ups were caused by the nucleus' recurring activity, not by collisions with asteroids, but he did not propose any specific active process.

Because the flare-ups were observed at large heliocentric distances, they could not be triggered by a suddenly elevated sublimation rate of water ice. Instead, the driver would have to have been explosions of carbon monoxide (possibly assisted by carbon dioxide). Unfortunately, as seen from Figure 9 of Paper 1, there were no obvious peaks on the carbon-monoxide production curve tempo-

Table 2
Cross-Sectional Area of Debris Released from C/1995 O1 in Post-Perihelion Flare-Ups

Flare-Up No.	Date of Flare-Up Onset (UT)	Time from Perihelion, $t - t_\pi$ (days)	Distance (AU) from		Phase Angle	Date of Flare-Up Peak ^a (UT)	Flare-Up Amplitude ^a (mag)	Debris Cross Section (10^6 km^2) in Field ^b	
			Sun	Earth				$34'' \times 34''$	10^{10} km^2
I	1998 Jan 8	+282	4.01	3.85	$14^\circ 2$	1998 Jan 11	0.8	0.88	0.93
II	May 8	+402	5.21	5.39	10.8	May 13	1.6	2.76	2.08
III	Aug 15	+501	6.13	6.28	9.3	Aug 17	1.4	1.53	0.99
IV	Dec 17	+625	7.21	7.26	7.8	Dec 20	1.1	1.68	0.94
V	1999 Apr 7	+736	8.11	8.16	7.0	1999 Apr 14	0.7	0.87	0.43

Note.

^a From Table 1 of Liller (2001).

^b Derived by normalizing flare-up amplitude; geometric albedo of 0.04 and surface brightness varying inversely with distance from the cluster's center of mass assumed.

rally coinciding with Liller's flare-up times in Figure 1. The single strongly elevated carbon-monoxide production rate, based on an observation made with an instrument onboard the Infrared Space Observatory (ISO) on 1998 April 6 (370 days after perihelion, when the comet was 4.9 AU from the Sun) precedes the flare-up II in Figure 1 by five weeks, and its origin is unclear. Thus, an intrinsic, carbon-monoxide driven event was not a primary trigger of the five (or six) post-perihelion flare-ups detected by Liller (2001).

Could each of the observed flare-ups contain in fact the debris of particular fragments in the cluster that collided with one another and broke up? In order to examine the implications of this hypothesis, let the masses of the colliding fragments be \mathcal{M}_i and \mathcal{M}_j , respectively, and let their relative velocity $(V_{\text{rel}})_{i,j}$ upon impact be high enough so that they both fracture (rather than bounce or stick together). In addition, let the slope of the size distribution of the debris generated by this collision equal the slope of the size distribution of the cluster's fragments, in which case the mass contained in the collisional debris

$$(\mathcal{M}_{\text{deb}})_{i,j} = \mathcal{M}_i + \mathcal{M}_j, \quad (36)$$

amounts to, in analogy to Equation (19),

$$\begin{aligned} (\mathcal{M}_{\text{deb}})_{i,j} &= \frac{5\pi}{6} \rho (D_{\text{max}})_{i,j}^3 \left[1 - \sqrt{\frac{(D_{\text{min}})_{i,j}}{(D_{\text{max}})_{i,j}}} \right] \\ &= 5 (\mathcal{M}_{\text{max}})_{i,j} \left[1 - \sqrt{\frac{(D_{\text{min}})_{i,j}}{(D_{\text{max}})_{i,j}}} \right], \end{aligned} \quad (37)$$

where $(D_{\text{max}})_{i,j}$ and $(D_{\text{min}})_{i,j}$ are, respectively, the diameters of the largest and smallest pieces in the debris of colliding fragments i and j , while $(\mathcal{M}_{\text{max}})_{i,j} = \frac{1}{6} \pi \rho (D_{\text{max}})_{i,j}^3$ is the mass of the largest piece. Furthermore, similarly to Equation (15), the cross-sectional area of the debris is

$$(X_{\text{deb}})_{i,j} = \frac{5\pi}{4} (D_{\text{max}})_{i,j}^2 \left[\sqrt{\frac{(D_{\text{max}})_{i,j}}{(D_{\text{min}})_{i,j}}} - 1 \right] \quad (38)$$

and, following Equation (17), the number of pieces in the debris field becomes

$$(N_{\text{deb}})_{i,j}^* = \left[\frac{(D_{\text{max}})_{i,j}}{(D_{\text{min}})_{i,j}} \right]^{\frac{5}{2}} = \left[1 + \frac{4(X_{\text{deb}})_{i,j}}{5\pi (D_{\text{max}})_{i,j}^2} \right]^5. \quad (39)$$

The five flare-ups reported by Liller (2001) are summarized in Table 2, the first eight columns of which are self-explanatory. Dropping the subscripts i and j , the critical quantity is the cross-sectional area X_{obs} , computed from a normalized amplitude of the flare-up's light curve by assuming a geometric albedo of 0.04 and allowing for the phase effect with the use of the Marcus (2007) modification of the Henyey-Greenstein scattering law. Observed in a $34'' \times 34''$ aperture, X_{obs} is listed in the penultimate column. In the last column it is scaled to a constant linear aperture of 10^5 km on a side, assuming that the surface brightness of the flare-up varied inversely as the distance from the cluster's center of light.

The tabulated cross-sectional data appear to be in a range of ~ 1 – 3 million km^2 in the $34''$ by $34''$ field, more than two orders of magnitude greater than the cross-sectional area of the comet's nucleus, based on the work by Szabó et al. (2012) and identified here with the total cross section of the proposed cluster of fragments. Some of this disparity is explained by the presence of optically effective, very fine dust in the flare-up debris, in contrast to the absence of fragments less than a few tens of meters across in the cluster once a flare-up fades away (Table 1). Accordingly, I adopt $D_{\text{min}} \simeq 0.3 \mu\text{m}$ in Equations (37) to (39), meaning it refers to the submicron-sized grains embedded in porous aggregate particles (e.g., Brownlee 1985)³ that are believed to make up much of the refractory mass of the fragments.

Another part of the disparity derives from the fact that a substantial increase in the surface area during the collisional fragmentation triggered off an increased production of carbon monoxide from the newly exposed surface, which necessarily entailed an increased production of dust. Evidence of CO-driven dust is implied by Liller's (2001) remark that the expansion rate of ejecta during the flare-ups exceeded 60 m s^{-1} , about two orders of magnitude higher than the impact velocity. This means that a flare-up's amplitude and the corresponding cross-sectional area X_{obs} consisted of at least two different components, X_{deb} referring only to the low-velocity mass. Since, as already noted, no spike was apparent in the carbon-monoxide production rate at the times of the flare-ups, the amplitude of the high-velocity compo-

³ Aggregate particles of this kind were recently reported to make up major part of the dust population of comet 67P/Churyumov-Gerasimenko (Della Corte et al. 2015; Merouane et al. 2016).

ment did not exceed the overall scatter in the CO production rate, which according to Table 19 of Paper 1 amounted to $10^{\pm 0.12}$, translating to a peak amplitude of 0.60 mag. Table 2 shows that Liller was able to detect flare-ups with an amplitude of 0.7 mag, so that a conservative estimate for a minimum detectable amplitude of the low-velocity component is ~ 0.1 mag, equivalent to a lower limit of the cross-sectional area of collisional debris of $X_{\text{lim}} \simeq 1 \times 10^3 \text{ km}^2$, which can now readily be equated with X_{deb} from Equation (38).

The issue now is how does X_{lim} compare with the cross-sectional area of the debris generated by a collision of two least massive fragments in the cluster, of a diameter D_\star . The mass of this debris is from Equation (36),

$$\mathcal{M}_{\text{deb}}(D_\star, D_\star) = 2\mathcal{M}(D_\star) = \frac{\pi}{3}\rho D_\star^3 \quad (40)$$

and, on the other hand, since $D_{\text{min}} \ll D_\star$, in terms of the largest piece of the debris, from Equation (37),

$$\mathcal{M}_{\text{deb}}(D_\star, D_\star) = \frac{5\pi}{6}\rho D_{\text{max}}^3. \quad (41)$$

Using these equations to eliminate D_{max} and given again that $D_{\text{min}} \ll D_\star$, one obtains for the cross-sectional area of the debris from Equation (38)

$$X_{\text{deb}}(D_\star, D_\star) = \left(\frac{5}{128}\right)^{\frac{1}{6}} \pi D_\star^{\frac{5}{2}} D_{\text{min}}^{-\frac{1}{2}}. \quad (42)$$

For the three scenarios from Table 1, the cross-sectional areas of the debris generated by a collision of the smallest fragments in the cluster are 10 km^2 for $D_0 = 8 \text{ km}$, 137 km^2 for $D_0 = 10 \text{ km}$, and 1116 km^2 for $D_0 = 12 \text{ km}$. These cross sections are all smaller than X_{lim} , which indicates that Liller (2001) missed these collisions because the triggered flare-ups had amplitudes that were too shallow to detect. Accordingly, Equation (35) needs to be corrected for incomplete statistics before the mean collisional rate (or the mean free time between collisions) based on Liller's flare-up observations can be employed to derive the dimensions of the cluster. A correction is to be applied in such a way that the smaller of any pair of colliding fragments should be allowed to have a diameter from the entire range of $D_\star \leq D < D_0$, whereas the larger one only from a range of $D_{\text{lim}} \leq D \leq D_0$; the task is to find D_{lim} such that a collision involving this fragment generates a debris whose cross-sectional area equals X_{lim} (Liller's detection limit); all collisions with a rate of $\dot{N}_{\text{coll}}^\star$, for which the diameter of the larger fragment is from a range $D_\star \leq D < D_{\text{lim}}$, are to be excluded from the count.

The procedure is very similar to the one used in Equations (40) to (42), starting now with a condition

$$\begin{aligned} \mathcal{M}_{\text{deb}}(D_{\text{lim}}, D_\star) &= \mathcal{M}(D_{\text{lim}}) + \mathcal{M}(D_\star) \\ &= \frac{\pi}{6}\rho D_{\text{lim}}^3 \left[1 + \left(\frac{D_\star}{D_{\text{lim}}}\right)^3 \right] \simeq \frac{\pi}{6}\rho D_{\text{lim}}^3 \end{aligned} \quad (43)$$

and resulting in

$$D_{\text{lim}} = 5^{-\frac{1}{15}} \left(\frac{4X_{\text{lim}}}{\pi}\right)^{\frac{2}{5}} D_{\text{min}}^{\frac{1}{5}} = 1.2 \text{ km}. \quad (44)$$

The collisional rate for Liller's observations becomes

$$(\dot{N}_{\text{coll}})_{\text{obs}} = \dot{N}_{\text{coll}} - \dot{N}_{\text{coll}}^\star, \quad (45)$$

where \dot{N}_{coll} is given by Equation (32) and the respective mean free time between collisions by Equation (35). The collisional rate $\dot{N}_{\text{coll}}^\star$ is similarly expressed as

$$\dot{N}_{\text{coll}}^\star = \nu^\star \langle \sigma^\star \rangle \langle V_{\text{rel}}^2 \rangle^{\frac{1}{2}} \quad (46)$$

where

$$\begin{aligned} \nu^\star &= \frac{6}{\pi D_{\text{frg}}^3} \left[\left(\frac{D_0}{D_\star}\right)^{\frac{5}{2}} - \left(\frac{D_0}{D_{\text{lim}}}\right)^{\frac{5}{2}} \right] \\ &= \frac{6\Psi_5}{\pi D_{\text{frg}}^3} \left(\frac{D_0}{D_\star}\right)^{\frac{5}{2}} \cdot \left(1 - \sqrt{\frac{D_\star}{D_{\text{lim}}}}\right) \end{aligned} \quad (47)$$

and, in analogy to Equation (31),

$$\langle \sigma^\star \rangle = \frac{5\pi}{2\Psi_5} D_\star^2 \left(1 + \frac{5\Psi_3^2}{9\Psi_5}\right), \quad (48)$$

with

$$\Psi_m = \sum_{k=0}^{m-1} \left(\frac{D_\star}{D_{\text{lim}}}\right)^{\frac{1}{2}k} = \frac{1 - \sqrt{(D_\star/D_{\text{lim}})^m}}{1 - \sqrt{D_\star/D_{\text{lim}}}} \quad (49)$$

The mean impact velocity is independent of fragment dimensions. Inserting from Equations (46), (34), (31), (33), (26), (47), (48), (19), and (15) into Equation (45), one finds that the collisional mean free time that is consistent with the observational limitations, $(\tau_{\text{coll}})_{\text{obs}} = (\dot{N}_{\text{coll}})_{\text{obs}}^{-1}$, equals

$$(\tau_{\text{coll}})_{\text{obs}} = \frac{\sqrt{5}}{30\eta\Phi} (G\rho X_{\text{frg}})^{-\frac{1}{2}} D_\star^{\frac{1}{4}} D_0^{-\frac{1}{4}} D_{\text{frg}}^{\frac{7}{2}}, \quad (50)$$

where $\eta \approx 1$, $G = 6.647 \times 10^7 \text{ cm}^3 \text{ g}^{-1} \text{ yr}^{-2}$ is the gravitational constant, and

$$\Phi = \frac{1}{\Gamma_5} \left(1 + \frac{5\Gamma_3^2}{9\Gamma_5}\right) - \left(1 + \frac{5\Psi_3^2}{9\Psi_5}\right) \cdot \left(1 - \sqrt{\frac{D_\star}{D_{\text{lim}}}}\right). \quad (51)$$

Equation (50) replaces (35) as an expression for the mean free time between collisions from the temporal distribution of the flare-ups observed by Liller (2001). Solving this equation for the cluster's collisional diameter D_{frg} , I list its values and the collisional parameters in Table 3 on the assumptions that $(\tau_{\text{coll}})_{\text{obs}} = 0.31 \text{ yr}$, $\eta = 1$, and $D_{\text{lim}} = 1.2 \text{ km}$. In addition to $\langle \sigma \rangle$, $\langle V_{\text{rel}}^2 \rangle^{1/2}$, and the true mean free time between collisions (i.e., both detected as the flare-ups and undetected), τ_{coll} , I also list four key parameters of the cluster of fragments from Table 1, as well as its average optical depth, Θ , defined as

$$\Theta = -\ln\left(1 - \frac{4X_{\text{frg}}}{\pi D_{\text{frg}}^2}\right), \quad (52)$$

and an average distance between the centers of neighboring fragments, s_{frg} , expressed by

$$s_{\text{frg}} = \left(\frac{\pi\sqrt{2}}{6}\right)^{\frac{1}{3}} \cdot \left(\frac{D_\star}{D_0}\right)^{\frac{5}{6}} D_{\text{frg}} = 0.9047 \left(\frac{D_\star}{D_0}\right)^{\frac{5}{6}} D_{\text{frg}}. \quad (53)$$

Table 3 shows that for any of the three potential principal fragment's diameters considered, the cluster's outer regions are exposed to the Sun's significant perturbations

at (and near) perihelion, as the collisional diameter then exceeds the stability diameter. It is expected that many fragments, especially at larger distances from the center of mass, entered markedly different trajectories after perihelion. This development should clearly increase the fragments' orbital diversity, thus the parameter η , and thereby give rise to a higher collisional rate than before perihelion, which is consistent with Liller's prime conclusion — the absence of major preperihelion flare-ups. Table 3 also suggests that given the validity of the size distribution of fragments and the detection limit, Liller observed, on the average, every fifth impact involving fragments larger than D_\star in diameter if the principal fragment was 12 km across, but only every seventeenth impact if it was 8 km across.

There are two additional more subtle effects mentioned by Liller (1997, 2001) that could likewise be explained by the proposed hypothesis of a cluster-like nucleus. At heliocentric distances r larger than ~ 2.5 AU Liller fits the quiescent phase of the light curve before and after perihelion by the same power law, r^{-n} , where $n = 2.55$. However, cursory inspection of the light curve reveals that the post-perihelion data marginally deviate from this slope, suggesting that the inner coma was fading at a slightly, but perceptibly, lower rate than it was brightening before perihelion. Yet, the intrinsic brightness was nearly 0.2 mag higher before perihelion. This behavior is qualitatively consistent with two properties implied by the proposed hypothesis: (i) the comet continued to lose mas-

sive fragments from its nucleus' cluster in the long run, hence it was brighter preperihelion; but (ii) the collisional rate was higher after perihelion (owing to the Sun's major perturbations of fragments' trajectories around perihelion), hence some of the new fragments lingered in the inner coma over longer periods of time after perihelion and the inner coma's brightness was fading somewhat less steeply. Indeed, the post-perihelion normalized brightness was lower near 2.5 AU but caught up with the preperihelion brightness by ~ 7 AU.

The other subtle peculiarity is Liller's (1997) reference to an apparent quasi-periodic variability in the preperihelion light curve, with an average period of 20 ± 4 days and a very small amplitude. It is noted from Table 3 that the *true* mean free time between *all* collisions was as short as ~ 7 days when one adopts a post-perihelion flare-up triggering collisional rate of 3.2 per year. However, I note that solutions consistent with a ~ 20 day periodicity require that the diameter D_0 of the principal fragment not exceed about 11 km under any circumstances. There are no solutions fitting this periodicity for the larger dimensions.

If the collisional rate was lower before perihelion, the 20-day period might fit with $D_{\text{lim}} \sim D_\star$. The dependence of a mean free time between collisions of fragments on a cross-sectional area of collisional debris and a limiting diameter D_{lim} is exhibited in Table 4 for the principal fragment's adopted diameters of 8 km and 10 km. The cross-sectional area of the debris is on the order of hundreds of square kilometers only, too low to detect with Liller's instrumentation, and an amplitude of the 20-day variations in the light curve, triggered by the periodic presence of collisional debris in the inner coma, is estimated to be merely on the order of thousandths of a magnitude. The statistically extracted amplitude of 0.1–0.2 mag, apparent from Figure 5 of Liller (1997), might be a product of the ensuing modest variations in the carbon-monoxide production and in the associated ejection of microscopic dust, as explained above.

Table 3

Constraints on Collisional Process in, and Dimensions of, Nucleus' Cluster of C/1995 O1

Parameter	Adopted Diameter D_0 of Principal Fragment		
	8 km	10 km	12 km
Cluster of Fragments at 1997 Apparition ^a			
Diameter of smallest fragment, D_\star (m)	24.4	70.0	162
Total number of fragments, $\mathcal{N}_{\text{frg}}^\star$ (10^5)	19.5	2.44	0.47
Total mass of fragments, \mathcal{M}_{frg} (10^{17} g)	5.07	9.60	16.0
Diameter of stability zone ^b , D_{st} (km)	173	214	254
Collisional Process in Cluster at 1997 Apparition ^{c,d}			
Cluster's collisional diameter, D_{frg} (km)	192	255	324
Number density of fragments, ν (km^{-3})	0.525	0.028	0.003
Average optical depth of cluster, Θ	0.161	0.088	0.054
Average distance between centers of fragments, s_{frg} (km)	1.39	3.69	8.11
Average collisional cross-sectional area of fragments, $\langle \sigma \rangle$ (km^2)	0.007	0.057	0.296
Average collisional relative (or impact) velocity of fragments, $(V_{\text{rel}}^2)^{1/2}$ (m s^{-1})	0.46	0.55	0.63
True mean free time between collisions (all events), τ_{coll} (days)	6.8	13.3	23.4

Notes.^a From Table 1.^b At perihelion.^c For bulk density of $\rho = 0.4 \text{ g cm}^{-3}$.^d For impact-velocity parameter of $\eta=1$, observed mean free time between collisions of $(\tau_{\text{coll}})_{\text{obs}} = 0.31 \text{ yr} = 114 \text{ days}$, and smaller fragment's minimum diameter of $D_{\text{lim}} = 1.2 \text{ km}$ for detectable flare-ups.**Table 4**

Preperihelion Mean Free Time Between Collisions of Fragments in Nucleus of C/1995 O1 as Function of Limiting Diameter, D_{lim} , and Cross-Sectional Area, X_{deb} , of Debris^a

Mean Free Time Between Collisions, $(\tau_{\text{coll}})_{\text{obs}}$ (days)	Adopted Diameter D_0 of Principal Fragment			
	8 km ^b		10 km ^c	
	D_{lim} (m)	$X_{\text{deb}}^{\text{d}}$ (km^2)	D_{lim} (m)	$X_{\text{deb}}^{\text{d}}$ (km^2)
16	81.2	200	91.8	270
18	95.6	300	109.2	416
20	110.7	431	124.9	582
22	126.6	603	142.1	804
24	143.1	818	159.7	1077

Notes.^a Other collisional parameters are the same as in Table 3.^b Diameter of smallest fragments is $D_\star = 24.4 \text{ m}$.^c Diameter of smallest fragments is $D_\star = 70.0 \text{ m}$.^d Total cross section of debris upon collision of two fragments with equal diameter D_{lim} ; derived from Equation (42) by replacing D_\star with D_{lim} .

10. RESULTING CONSTRAINTS ON DIMENSIONS OF PRINCIPAL FRAGMENT

Up to Table 3, I executed all computations on three different assumptions regarding the diameter of the principal fragment — 8 km, 10 km, and 12 km. The tests carried out in Sections 2–9 and further evidence allow now one to narrow down the width of the appropriate size span. In the following I separately discuss the various criteria in terms of the preferences for particular segments of the 4-km wide range of the fragment’s diameter.

10.1. *Nongravitational Acceleration*

The conservation-of-momentum criterion is of fundamental significance, because it is on the strength of this evidence that the hypothesis of the comet’s nucleus in the form of a compact cluster of massive fragments has been contemplated as the *only* credible scenario. The estimated disparity between the derived orbit-integrated nongravitational acceleration and the one expected on the assumption that the nucleus was a single body of the same cross-sectional area amounts to more than two orders of magnitude in terms of the momentum, or a little less than a factor of 10 in terms of the nucleus’ size. The estimated uncertainty by a factor of 3–4 in the efficiency of the momentum applied by outgassing is equivalent to an uncertainty by a factor of only ~ 1.5 in the linear dimension. The principal fragment’s diameter of 12 km refers to a momentum transfer so efficient that it is barely at a limit of feasibility; the lower end of the 4-km range for the principal fragment’s diameter (Table 3) should accordingly be assigned a much higher probability.

10.2. *High-Resolution Imaging*

The high resolution imaging, especially with the HST, provides a strong argument in favor of a very tight cluster. Because the nucleus’ image peaks up rather sharply, its overall dimension can extend at most over just two pixels of the HST’s WFPC-2 sensor, each of which corresponds to 90–100 km across on four of the six analyzed preperihelion images between 1995 October 23 and 1996 October 17 (Sekanina 1999a), thus limiting the cluster’s diameter to about 200 km at the extreme. It is therefore *only* the lower end of the principal fragment’s range of dimensions that passes this test (Table 3).

10.3. *Stellar Occultation*

Fernández et al. (1999) published the results of their campaign to observe an occultation by the comet’s nucleus of the star PPM200723 on 1996 October 5. The event’s light curve, obtained by apparently the only team that reported a positive detection, was *V shaped*, without any step-like variations or a trough implied by an occulting monolithic body between the ingress and egress of the star. Indeed, the best models offered by Fernández et al. included those with an occultation chord of zero length, even though the degree of dimming indicated the star’s complete disappearance behind the comet at the time of maximum drop in the count rate. Accordingly, the authors could only conclude that the nucleus was less than 60 km in diameter, an estimate that is too low and inconsistent with Szabó et al.’s (2012) result. For the nucleus in the form of a compact cluster of massive fragments one expects a light curve that should be

fairly smooth and essentially trough-free. The smaller the principal fragment’s size, the more consistent the cluster scenario is with the apparent absence of a trough. In spite of the uncertainties involved, the event appears to have lasted 40 ± 5 s, suggesting the cluster’s collisional diameter of 204 ± 26 km, implying the principal fragment 8.4 ± 0.8 km across.

10.4. *Sun’s Perturbations of Cluster Fragments’ Orbits*

Because the size of the zone of stability determined in Section 4 is approximate, all that can be stated about the perturbation effects of the Sun near the 1997 perihelion is that they should have made the orbits of fragments near the outer boundary of the cluster essentially chaotic. As seen from Table 3, the extent of this instability increases with the size of the principal fragment more steeply than linearly. As a corollary, the collisional rate among the fragments in the cluster should have gotten augmented after perihelion regardless of the principal fragment’s size, as implied by Liller’s (2001) results.

10.5. *Properties of Original Nucleus*

Listed in Table 1, the fundamental parameters of the original nucleus that is presumed to have begun to fragment at the time of close encounter with Jupiter in the year -2251 (or 2252 BCE) suggest, to a degree, that the principal fragment’s diameter of 8 km is more likely than 12 km. Statistically, an original nucleus 22 km in diameter has a higher probability of occurrence than a nucleus 33 km in diameter. Similarly, the fragments would have stayed tighter together (and the cluster would have had better gravitational stability) at a lower rotation velocity (i.e., a smaller nucleus). The lower end of the size range is also more plausible because the central gravitational pressure is than more in line with the compressive strength, estimated for 67P at 1–3 kPa by Basilevsky et al. (2016) and its upper limit at only 1.5 kPa by Groussin et al. (2015). The latter team pointed out that diagenesis may then be initiated in the interior of the comet’s nucleus. The probability of this process to have commenced in C/1995 O1 increases with the square of the size of the original nucleus. On the other hand, the tensile strength needed for C/1995 O1 to begin to fragment at the Jovian encounter just matched the lower end of the range reported for 67P, thus making a larger original nucleus slightly more likely but by no means indispensable.

10.6. *Distance Between Fragments in the Cluster*

It is noted from Table 3 that s_{frg} , an average distance between the centers of fragments, is in each of the three cases shorter than the diameter of the principal fragment. In fact, $s_{\text{frg}} \leq D_{\otimes} \leq D_0$ and the number of fragments whose diameters are equal to or greater than D_{\otimes} is

$$\mathcal{N}_{\text{frg}}(D_{\otimes}) < \left(\frac{D_0}{s_{\text{frg}}} \right)^{\frac{5}{2}}. \quad (54)$$

It turns out that nearly 80 most massive fragments comply with this condition when the principal fragment is 8 km across, 12 fragments when it is 10 km across, but only the principal fragment and the second most massive fragment when 12 km across. This exercise provides a yet another argument for a high chance, if not inevitability, of frequent collisions among fragments in the cluster.

In practice, this means that near the cluster's center of mass, where the principal fragment and perhaps some other major fragments should reside, the number density of fragments is much lower than the average, probably not more than $\sim 10^{-3}$ per km^3 , given that the volumes of the 8 km, 10 km, and 12 km fragments are, respectively, 268 km^3 , 524 km^3 , and 905 km^3 . Collisions of the principal fragment with other fairly large fragments are likely to account for a fraction of the post-perihelion collisional rate derived from Liller's (2001) observations.

10.7. Impact Velocity and Collisional Rate

Table 3 shows that an average impact velocity depends only moderately on the principal fragment's dimensions and is close to 0.5 m s^{-1} , high enough to assure continuing fracture (rather than bouncing) of the initial tidally-generated fragments of the original nucleus. This expectation is based on the assumption that, on the average, the impact velocities crudely equal in magnitude the velocities of fragments about the center of mass of the cluster in nearly circular orbits. This is a plausible assumption, if the fragments' motions are essentially random. One deals here with a self-feeding mechanism: the more often the collisions occur, the more random the orbits become; the stochastic nature is also aided by the Sun's perturbations, especially near perihelion.

Two further post-perihelion flare-ups were reported in gaps of Liller's (2001) observing run, one in late August 1997 (McCarthy et al. 2007), four months before Liller's first flare-up; the other in mid-October 1999 (Pearce 1999; Griffin & Bos 1999), six months after Liller's last flare-up. If included, they would increase $(\tau_{\text{coll}})_{\text{obs}}$ in Equation (50) from 0.31 yr to 0.36 yr, which would change the cluster's collisional diameter by $\sim 4\%$, rather an insignificant effect.

10.8. A Verdict

In summary, the lower end of the range of the principal fragment's size — a diameter of 8–9 km and a mass of $1.1\text{--}1.5 \times 10^{17} \text{ g}$ — comes out from this discussion as the preferred one by far, because of the arguments presented primarily in Sections 10.1–10.2, but also in 10.3, and, in part, in 10.5. The cluster of fragments, some $210 \pm 20 \text{ km}$ in diameter, and the pre-encounter nucleus are described by the data that can be interpolated from Tables 1 and 3.

A complete summary of the cluster's adopted parameters for the principal fragment's representative diameter of 8.5 km is tabulated in Section 12. I may point out that from their nongravitational model for comet motions and independently determined nongravitational parameters (with the radial and transverse components only), Sosa & Fernández (2011) derived for the nucleus of C/1995 O1 a diameter of 9.6 km and a mass of $1.9 \times 10^{17} \text{ g}$, remarkably close to the present results for the principal fragment.

For a cluster-like nucleus, many observed properties of C/1995 O1 (such as the rotation vector, albedo, activity variations, complex dust-coma morphology and its evolution, striation pattern in the tail, gravitationally-bound satellite, etc.) will require a profound re-interpretation. While a complete overhaul of the large body of models that address these issues is outside the scope of this paper, I pay attention to the problem of a satellite, a topic that turns out to be particularly closely related to the proposed paradigm of a compact cluster.

It is the orbital instability of fragments in the outer reaches of the cluster — which will from now on be referred to as a *primary (or main) nucleus' cluster* or just a *primary* — that lends legitimacy to such a link. This instability virtually warrants that, from time to time, a fragment or a subcluster of fragments escapes from the primary, thus contributing to a population of boulder-sized debris scattered over an expanding volume of hundreds or thousands of kilometers across around the primary. A vast majority of individual fragments are too feeble to detect even with the HST, but subclusters of fragments should over a limited period of time show up as faint companions. This likely scenario invites a suggestion to conduct a computer search for such companions in the HST images.

11. ON THE OCCURRENCE OF COMPANION NUCLEI

My presentation of evidence on a major satellite orbiting the primary nucleus of C/1995 O1 (Sekanina 1999b) has been a subject to controversy ever since, in part because the reported detection — in five preperihelion images (in 1996 May–October) taken with the HST Wide-Field Planetary Camera 2 (WFPC-2; imaging scale of $0''.0455$ per pixel) through an F675W filter — was made digitally; no companion was readily apparent in the images when inspected visually. The applied computer procedure, based on an iterative least-squares differential-correction technique, was described in detail elsewhere (Sekanina 1995; an upgraded version in Sekanina 1999a). The identification of this object as a satellite gravitationally bound to the main nucleus was based on the assumption that the primary was at least $3.4 \times 10^{19} \text{ g}$ in mass (i.e., 55 km across at a bulk density of 0.4 g cm^{-3}) and that therefore the radius of a gravitationally stable zone around the nucleus was at least 370 km at perihelion [Equation (9) gives $\sim 350 \text{ km}$ with $h_0 = 0.1$]. The satellite, with its average projected distance of $\sim 180 \text{ km}$ from the primary, was safely inside the stability zone unless it was in each of the five images located near the line of sight, a statistically unlikely scenario.

With a cluster of fragments replacing the solid nucleus, the situation is rather different. The stability zone being at perihelion less than 100 km in radius (Table 1), the companion would have been located outside the zone at heliocentric distances of up to at least $\sim 2 \text{ AU}$, i.e., over a period of $\gtrsim 200$ days around perihelion. (On the other hand, the companion should have remained inside the Hill sphere at all times.) Dynamically, it is possible but unlikely that these conditions would have sufficed for the satellite to escape along an unbound orbit over a period of several months. It does not appear it happened, if the five satellite images refer to the same object. However, if the companion's existence dated back to the close encounter with Jupiter, the 1997 perihelion was already a second instance of severe solar perturbations.⁴

11.1. Doubts on the Existence of the Satellite

In the past, dynamical issues were not at the focus of a controversy on whether the satellite (or companion) did in fact exist. The doubts were expressed because of

⁴ This statement does not apply to the published evidence on the satellite based on the preperihelion observations (Sekanina 1999b); however, as explained in Section 11.4, at least one major companion was likewise detected in each of three post-perihelion HST images.

the conditions under which the satellite’s signature was extracted from the HST images, in the presence of large amounts of dust and its uneven spatial distribution in the inner coma of C/1995 O1.

Weaver & Lamy (1999) questioned the detection on the grounds that the excess signal attributed to the satellite is “due to inadequate modeling of the complex coma morphology and/or temporal variability.” They also warned that the HST’s CCD arrays “are imperfect detectors whose noise does not always obey the laws of counting statistics,” a problem that of course is model independent. In a follow-up paper, Weaver et al. (1999) reported that they found no companions in the post-perihelion HST images taken in 1997–1998 with a Space Telescope Imaging Spectrograph (STIS), but admitted that their detection threshold was rather limited; I return to this topic in Section 11.4. In his review of the topics related to the size and activity of C/1995 O1, Fernández (2002) responded to the report of the satellite more suavely, pointing out that the detection “remains controversial because of the difficulty in understanding the inner coma’s brightness distribution.”

11.2. Evidence Supporting a Companion’s Existence

A series of images of the comet was obtained on 1996 September 30 with a newly commissioned adaptive optics system PUEO (also referred to as Bonnette, AOB) on the Canada–France–Hawaii 3.6-m f/8 telescope on Mauna Kea (Rigaut et al. 1998).⁵ When deconvolved, the images showed a “knot of material” $0''.15$ north of the nucleus, at a position close to that of the reported satellite in an HST image taken a week earlier (Sekanina 1999b).

Marchis et al. (1999) used another adaptive optics system, ADONIS, on the ESO 3.6-m telescope at La Silla, Chile, to take the comet’s images on 1996 November 6 and 1997 January 15; in their deconvolved frames, the central peak is clearly resolved into two maxima of uneven brightness, the fainter separated from the brighter by $0''.23$ at a position angle of $102^\circ \pm 4^\circ$ in November and by $0''.36$ at $78^\circ \pm 5^\circ$ in January. Marchis et al. considered three interpretations for the secondary peak, including a companion nucleus, and concluded that *based on their observations alone they remained undecided as to whether the feature on either night was a near-nucleus footprint of a jet or a secondary nucleus, but when combining their results with the findings by others, the scenario involving “a double nucleus . . . seems to be the most likely.”* These authors also noted that in both cases the compact feature projected close enough to the nucleus to qualify as a gravitationally bound object and that its position angles did not coincide with the directions of the jets observed at 0° – 30° , 75° – 95° , 115° – 135° , and 240° – 260° in November, and at 0° – 40° and 90° – 130° in January.

11.3. Arguments and Counter-Arguments Based on Modeling Dust-Coma Morphology

In a study of the dust-coma morphology of C/1995 O1 (Sekanina 1998), I pointed out that — given the comet’s well determined spin vector — a system of about eight *evenly separated* halos in the southeastern quadrant of the coma, prominently apparent in the comet’s images

from 1997 late February and early March, could not (unlike the halos in the southwestern quadrant in the same images) be modeled as dust ejecta from any source on the nucleus (not even on the antisunward side) and that one has to admit that the observed morphology is a product of dust ejecta from *two independent objects*⁶ of different axial orientation, thus providing further support for the existence of a companion. This same conclusion was independently reached by Vasundhara & Chakraborty (1999) in their morphological study of C/1995 O1, and the argument was also raised by Marchis et al. (1999).

On the other hand, Samarasinha (2000) argued that the discussed system of dust halos in the southeastern quadrant could in fact be successfully modeled as a product of an extended emission region (about 40° wide) on the surface of the main nucleus. Unfortunately, in an effort to demonstrate his idea, he applied an approach that ignored effects of solar radiation pressure, an impermissible omission. As it turns out, an integrated contribution from the radiation pressure became comparable in magnitude to the contribution from the ejection velocity — the variable that Samarasinha did account for in his model — not later than in the course of the third rotation (of the eight involved), but possibly earlier, depending on the projected ejection velocity and the radiation pressure acceleration of the submicron-sized grains that made up the features’ outer boundaries. An even distribution of the consecutive halos in Samarasinha’s (2000) model is an artifact of his neglect of radiation pressure; its incorporation into the model would compress the halos into a bright, extended blob in the southeastern quadrant of the nucleus. No such feature is apparent in the comet’s pertinent images, suggesting that the proposed active region of enormous extent did not exist.

In general, the morphology of a dust-coma feature that is produced by an extended source is modeled by using a collection of densely distributed point sources (Sekanina 1987); this technique would certainly have been applied to C/1995 O1 should it have been of any help.

11.4. Companions in HST’s STIS Images

In Section 11.1 I remarked on three post-perihelion images of C/1995 O1 taken in 1997–1998 with a then newly installed STIS instrument on board the HST as well as on Weaver et al.’s (1999) report of their non-detection of any companions. In this paper I present for the first time the results of my subsequent search for companions in these images, using the technique that was previously applied to the HST’s preperihelion WFPC-2 images (Sekanina 1999a, 1999b). The advantages of STIS over WFPC-2 are a higher quantum efficiency and a lower readout noise of its CCD array and much broader imaging passbands, thus reaching objects ~ 1.5 mag fainter. On the other hand, STIS is less well photometrically defined than WFPC-2, with its point spread function expected to degrade approximately 30% near the boundary of the field of view (Baum 1996).

11.4.1. Method of CCD signature extraction

The observed surface brightness distribution was available as an array of pixel signals measured in CCD analog-to-digital intensity units (ADU px^{-2}), with each pixel

⁵ For the comet’s images and their description, see http://www.cfht.hawaii.edu/Instruments/Imaging/AOB/best_pictures.html.

⁶ More accurately, from *at least* two independent objects.

Table 5Primary Nucleus and Major Companions^a Digitally Detected in HST Images Taken in 1995–1998 (with Law A for Extended Source)

Instrument	Time of Observation (UT)	Equivalent Diameter (km) of		Projected Distance (km)	Projected Angular Distance	Position Angle	Number of Point Sources	Mean Residual (ADU) ^b	Exp. Time (s)
		Primary	Companion						
WFPC-2	1995 Oct 23.27	75.8 ± 0.6	2	±2.1	180
	1996 May 20.45	75.1 ± 0.8	39.9 ± 1.6	163 ± 8	0''0612 ± 0''0030	351°2 ± 2°6	4	±1.9	20
	Jun 22.49	72.0 ± 0.4	32.0 ± 0.9	211 ± 4	0.0965 ± 0.0019	314.0 ± 1.1	6	±2.7	20
	Jul 25.60	69.3 ± 0.3	32.3 ± 0.6	184 ± 2	0.0925 ± 0.0011	3.0 ± 0.6	9	±1.7	16
	Sept 23.18	72.7 ± 0.5	32.9 ± 1.5	161 ± 5	0.0751 ± 0.0025	1.5 ± 1.9	6	±2.4	14
	Oct 17.63 ^c	73.9 ± 0.8	37.1 ± 1.0	177 ± 3	0.0828 ± 0.0015	131.7 ± 1.1			
STIS	1997 Aug 27.17	68.1 ± 0.6	32.8 ± 1.4	222 ± 3	0.1006 ± 0.0015	119.8 ± 1.0	12	±1.5	20
	Nov 11.80	71.6 ± 0.3	30.3 ± 1.0	168 ± 4	0.0775 ± 0.0017	177.3 ± 4.6	18	±4.1	11
	1998 Feb 19.55	72.5 ± 0.2	28.1 ± 1.6	230 ± 4	0.1063 ± 0.0019	215.9 ± 1.1			
			25.5 ± 0.8	202 ± 4	0.0841 ± 0.0016	336.8 ± 0.8	13	±3.3	22
			36.1 ± 0.6	254 ± 3	0.0795 ± 0.0010	28.5 ± 0.6	11	±2.7	35
			23.5 ± 1.6	573 ± 9	0.1796 ± 0.0029	18.1 ± 1.3			
			22.2 ± 1.0	411 ± 12	0.1290 ± 0.0037	347.3 ± 1.6			

Notes.^a Whose integrated signal is greater than 8% of the primary nucleus' signal (i.e., companions with equivalent diameters greater than ~20 km).^b ADU = analog-to-digital units, measuring pixel signals; for WFPC-2 images these residuals are corrections to Table II of Sekanina (1999a).^c This is a new solution based on a corrected exposure time; an average of the six 1995–1996 determinations has now changed to 73.1 ± 2.4 km.

0''0508 on a side. A background noise of 3 ADU px⁻² was subtracted. The net pixel signals were assumed to consist of a convolved sum of three contributions: (i) from one or more extended sources (to model the coma's complex morphology); (ii) from the primary nucleus (dominant point source); and (iii) from additional point sources, some of which could represent genuine companions (nuclear fragments or their clusters), while others are fictitious spots of light of instrumental or unknown origin.

Employing its surface brightness map for STIS images, the point spread function (PSF) was approximated by a quasi-Gaussian law with a symmetrical surface brightness distribution $b_{\text{psf}}(X, Y)$, which at a point $\{X, Y\}$, whose distance from the PSF's peak at $\{X_\star, Y_\star\}$ equaled $\Delta X = X - X_\star$ and $\Delta Y = Y - Y_\star$, was expressed as

$$b_{\text{psf}}(X, Y) = b_\star \exp \left[- \left(\frac{\Delta X^2 + \Delta Y^2}{2\sigma_{\text{psf}}^2} \right)^{\nu_{\text{psf}}} \right], \quad (55)$$

where σ_{psf} is the PSF's dispersion parameter, ν_{psf} is a dimensionless constant, and $b_\star = b_{\text{psf}}(X_\star, Y_\star)$ is the peak surface brightness. The integrated brightness I_\star of the point source is then

$$I_\star = 2\pi b_\star \sigma_{\text{psf}}^2 \nu_{\text{psf}}^{-1} \Gamma(\nu_{\text{psf}}^{-1}), \quad (56)$$

where $\Gamma(z)$ denotes the Gamma function of argument z . For the long-pass (LP) filter the parametric values are $\sigma_{\text{psf}} = 0.1461$ px and $\nu_{\text{psf}} = 0.3034$, so that I_\star in ADU is

$$I_\star = 1.181 b_\star, \quad (57)$$

where b_\star is in ADU px⁻². Each point source is fully described by three constants: X_\star , Y_\star , and I_\star .

A surface brightness distribution in extended sources, $b_{\text{ext}}(X, Y)$, was approximated (after its convolution with the PSF) by an ellipsoidal power law (referred to as law A in Sekanina 1999a, 1999b), which allowed for a deviation of the peak's location in the ellipsoid's center, described by $\{X_{\text{ext}}, Y_{\text{ext}}\}$, from the origin of the coordinate system,

as well as for anisotropy and an arbitrary orientation, the latter defined by an angle θ_{ext} in the direction of the most gentle rate of signal decline from the peak:

$$b_{\text{ext}}(X, Y) = \frac{b_0}{1 + \left[\left(\frac{\Delta X}{\sigma_x} \right)^2 + \left(\frac{\Delta Y}{\sigma_y} \right)^2 \right]^{\frac{1}{2}\nu_{\text{ext}}}}, \quad (58)$$

where

$$\begin{pmatrix} \Delta X \\ \Delta Y \end{pmatrix} = \begin{pmatrix} \cos \theta_{\text{ext}} & \sin \theta_{\text{ext}} \\ -\sin \theta_{\text{ext}} & \cos \theta_{\text{ext}} \end{pmatrix} \cdot \begin{pmatrix} X - X_{\text{ext}} \\ Y - Y_{\text{ext}} \end{pmatrix}, \quad (59)$$

σ_x and σ_y are the maximum and minimum dispersions of the surface brightness distribution along, respectively, the X and Y axes, and ν_{ext} is the exponent of the power law. Each extended source is fully described by seven independent constants: X_{ext} , Y_{ext} , σ_x , σ_y , b_0 , ν_{ext} , and θ_{ext} .

To summarize, in a search for N_{pt} point sources and N_{ext} extended sources, the deconvolving procedure's optimization least-squares differential-correction technique was required to iteratively solve for $3N_{\text{pt}} + 7N_{\text{ext}}$ parameters; typically, signals in 157 pixels were fitted.

11.4.2. Results

The extracted dimensions of the primary nucleus and some results of a search for companions in the STIS images are presented in Table 5 together with the partially revised results of a previous analysis of the preperihelion WFPC-2 images⁷ (Sekanina 1999a, 1999b). The tabulated numbers and experience with the fitting procedure offer these conclusions: (1) The fitted dimensions of the primary nucleus are remarkably consistent over

⁷ The image from 1996 October 17 was reanalyzed, because only after the original papers (Sekanina 1999a, 1999b) were accepted for publication it became known that the initially announced exposure time was incorrect (see Table I in Sekanina 1999a). In addition, recent inspection of the computer runs revealed that the mean residuals in Table II of Sekanina (1999a) were inadvertently multiplied by a factor of 10, an error that has now been corrected in Table 5.

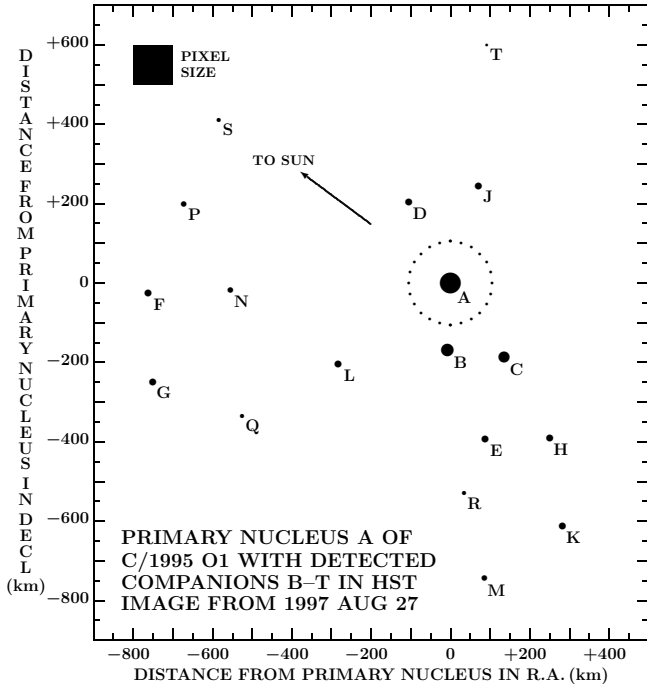


Figure 2. Spatial distribution of detected companions B–T relative to the primary nucleus A of comet C/1995 O1 in projection onto the plane of the sky on 1997 August 27. The size of the circles is to scale on the assumption of infinite opacity, i.e., for an equivalent diameter listed in Table 6. The dotted circle shows the dimensions of the compact cluster of fragments that represents the primary nucleus A, as adopted in Section 10.8. The diameters of the companion nuclei should be adjusted proportionately, if they too are judged to consist of compact clusters of fragments. Unlike dust jets, most companions project relative to the primary nucleus in directions that are far from the direction to the Sun.

the orbital arc of 28 months, with an *equivalent diameter* (measuring the observed cross-sectional area) averaging 73.1 ± 2.4 km, within 0.4σ of the result derived by Szabó et al. (2012); (2) introduction of a second extended source in the solutions consistently failed to improve the fit to the distribution of dust in the coma, implying — together with a low rms residual of about ± 2 –4 ADU — that the employed distribution function given by Equation (58) provided an adequate approximation; (3) a large number of companion nuclei was detected with both instruments, the larger post-perihelion numbers being owing in part to the STIS instrument’s higher sensitivity; (4) as shown in an example in Figure 2, most companion nuclei were not, unlike dust jets, located in directions close to that of the Sun⁸ and were not concentrated densely along particular lines, thus making their interpretation as phenomena that were closely related to dust jets quite unlikely; (5) as further documented by Tables 6–8, the brighter companions had an extremely high signal-to-noise ratio close to or exceeding 10, and only for a few of the tabulated objects could their existence be readily questioned, in particular, the companions R, S, and T in Table 6, N’ in Table 7, and K’’ and L’’ in Table 8.

⁸ Contained in the 90° sector centered on the projected sunward direction are only five of the 17 companions in the 1997 August 27 image; only five of the 12 companions in the 1997 November 11 image; and — astonishingly — none of the 10 companions in the 1998 February 19 image.

Table 6
Signals and Equivalent Diameters of Primary Nucleus and Companions in the STIS Image of 1997 August 27

Object	PSF Signal in Units of		S/N Ratio	Equivalent Diameter (km)
	ADU/s	Primary’s Signal		
A	3626 ± 68	53.3	68.1 ± 0.6
B	717 ± 48	0.198 ± 0.014	14.9	30.3 ± 1.0
C	617 ± 72	0.170 ± 0.020	8.6	28.1 ± 1.6
D	291 ± 35	0.080 ± 0.010	8.3	19.3 ± 1.2
E	265 ± 35	0.073 ± 0.010	7.6	18.4 ± 1.2
F	245 ± 20	0.068 ± 0.006	12.3	17.7 ± 0.7
G	245 ± 36	0.068 ± 0.010	6.8	17.7 ± 1.3
H	240 ± 28	0.066 ± 0.008	8.6	17.5 ± 1.0
J	234 ± 25	0.065 ± 0.007	9.4	17.3 ± 0.9
K	225 ± 21	0.062 ± 0.006	10.7	17.0 ± 0.8
L	195 ± 28	0.054 ± 0.008	7.0	15.8 ± 1.1
M	161 ± 21	0.045 ± 0.006	7.7	14.3 ± 0.9
N	156 ± 20	0.043 ± 0.005	7.8	14.1 ± 0.9
P	150 ± 19	0.041 ± 0.005	7.9	13.9 ± 0.9
Q	122 ± 20	0.034 ± 0.006	6.1	12.5 ± 1.0
R	99 ± 34	0.027 ± 0.009	2.9	11.3 ± 1.9
S	71 ± 28	0.020 ± 0.008	2.5	9.5 ± 1.9
T	52 ± 20	0.014 ± 0.005	2.6	8.2 ± 1.6

The primary nucleus (i.e., the compact cluster of fragments proposed to make it up) is marked A in all three STIS images; B–T are the companion nuclei detected in the image taken on 1997 August 27 (Table 6); B’–N’ the companions detected in the image of 1997 November 11 (Table 7); and B’’–L’’ the companions in the image of 1998 February 19. As pointed out, the existence of the objects R, S, T, N’, K’’, and L’’ is questionable; the existence of G’, H’, and J’’ is somewhat uncertain.

It may be significant that the bright companion in the image of 1996 October 17 (Table 5), taken only 20 days before the ESO observation that we referred to in Section 11.2, is located at a position angle that differs from that in the ESO image by less than 4σ and at a comparable angular distance from the primary nucleus. The positional difference may be due in part to the companion’s motion in the course of the 20 days, in part to effects introduced by the heavy processing of the ESO image.

Table 7
Signals and Equivalent Diameters of Primary Nucleus and Companions in the STIS Image of 1997 November 11

Object	PSF Signal in Units of		S/N Ratio	Equivalent Diameter (km)
	ADU/s	Primary’s Signal		
A	1856 ± 13	142.8	71.6 ± 0.3
B’	236 ± 15	0.127 ± 0.008	15.7	25.5 ± 0.8
C’	133 ± 9	0.071 ± 0.005	14.8	19.2 ± 0.6
D’	117 ± 11	0.063 ± 0.006	10.6	18.0 ± 0.8
E’	90 ± 9	0.049 ± 0.005	10.0	15.8 ± 0.8
F’	73 ± 17	0.039 ± 0.009	4.3	14.2 ± 1.7
G’	60 ± 10	0.032 ± 0.005	6.0	12.9 ± 1.1
H’	54 ± 10	0.029 ± 0.006	5.4	12.2 ± 1.1
J’	50 ± 8	0.027 ± 0.004	6.8	11.8 ± 0.9
K’	46 ± 8	0.025 ± 0.004	5.8	11.3 ± 1.0
L’	42 ± 8	0.023 ± 0.004	5.3	10.8 ± 1.0
M’	35 ± 8	0.019 ± 0.004	4.4	9.8 ± 1.1
N’	18 ± 7	0.010 ± 0.004	2.6	7.1 ± 1.4

Table 8

Signals and Equivalent Diameters of Primary Nucleus and Companions in the STIS Image of 1998 February 19

Object	PSF Signal in Units of		S/N Ratio	Equivalent Diameter (km)
	ADU/s	Primary's Signal		
A	707 ± 4	176.8	72.5 ± 0.2
B''	174 ± 6	0.246 ± 0.009	29.0	36.0 ± 0.6
C''	74 ± 10	0.105 ± 0.009	7.4	23.5 ± 1.6
D''	66 ± 6	0.093 ± 0.008	11.0	22.2 ± 1.0
E''	36 ± 4	0.051 ± 0.006	8.0	16.4 ± 0.9
F''	36 ± 5	0.051 ± 0.007	7.2	16.4 ± 1.1
G''	31 ± 10	0.044 ± 0.014	3.1	15.2 ± 2.4
H''	29 ± 8	0.041 ± 0.011	3.6	14.7 ± 2.0
J''	16 ± 5	0.023 ± 0.007	3.2	10.9 ± 1.7
K''	12 ± 4	0.017 ± 0.006	3.0	9.4 ± 1.6
L''	7 ± 4	0.010 ± 0.006	1.8	7.2 ± 2.0

A list of all detected companion nuclei is in the order of increasing projected distance from the primary nucleus presented in Table 9. Since the radius of the stability zone defined by Equation (9) (with $h_0 = 0.1$ and the primary nucleus' mass of 6×10^{17} g; cf. Section 12) amounted to 250 km for the image of 1997 August 27, to 340 km for the image of 1997 November 11, and to 450 km for the image of 1998 February 19, only 3–6 innermost companions were likely to have been, on any of the three dates, located inside the stability zone of the primary. On the other hand, all companions were located deep inside the Hill sphere of the primary nucleus — whose radii at the three times were between 1700 km and 3100 km — unless the distances were in each image strongly foreshortened. This result suggests that the primary nucleus was still likely to exert much influence over the motions of many if not all of the detected companions at the times of observation.

Table 9

Projected Locations of Detected Companions Relative to Primary Nucleus on the STIS Images

Companion	Detection in Image Taken on	Relative to Primary Nucleus in Projection		
		Angular Separation	Separation at Comet (km)	Position Angle
B	1997 Aug 27	0''.0775 ± 0''.0017	168 ± 4	177°3 ± 4°6
B'	1997 Nov 11	0.0841 ± 0.0016	202 ± 4	336.8 ± 0.8
D	1997 Aug 27	0.1062 ± 0.0042	230 ± 9	27.1 ± 1.1
C	1997 Aug 27	0.1063 ± 0.0019	231 ± 4	215.9 ± 1.1
J	1997 Aug 27	0.1169 ± 0.0033	253 ± 7	343.9 ± 2.7
B''	1998 Feb 19	0.0795 ± 0.0010	254 ± 3	28.5 ± 0.6
C'	1997 Nov 11	0.1174 ± 0.0023	281 ± 6	183.2 ± 1.0
H'	1997 Nov 11	0.1194 ± 0.0060	286 ± 14	130.1 ± 2.6
D'	1997 Nov 11	0.1232 ± 0.0033	295 ± 8	90.6 ± 1.6
K'	1997 Nov 11	0.1297 ± 0.0108	311 ± 26	239.3 ± 2.4
E'	1997 Nov 11	0.1381 ± 0.0042	331 ± 10	295.4 ± 1.6
L	1997 Aug 27	0.1608 ± 0.0039	349 ± 8	125.8 ± 1.3
[H'']	1998 Feb 19	0.1181 ± 0.0093	377 ± 30	318.2 ± 3.1
E''	1998 Feb 19	0.1194 ± 0.0057	381 ± 18	106.8 ± 1.7
E	1997 Aug 27	0.1857 ± 0.0039	403 ± 8	192.5 ± 2.3
D''	1998 Feb 19	0.1290 ± 0.0037	411 ± 12	347.3 ± 1.6
G'	1997 Nov 11	0.1747 ± 0.0091	419 ± 22	338.1 ± 1.3
H	1997 Aug 27	0.2139 ± 0.0029	464 ± 6	212.6 ± 0.9
(R)	1997 Aug 27	0.2441 ± 0.0086	529 ± 19	183.7 ± 2.8
N	1997 Aug 27	0.2557 ± 0.0059	554 ± 13	91.8 ± 0.8
M'	1997 Nov 11	0.2331 ± 0.0094	559 ± 23	111.0 ± 2.3
C''	1998 Feb 19	0.1796 ± 0.0029	573 ± 9	18.1 ± 1.3
(T)	1997 Aug 27	0.2804 ± 0.0137	608 ± 30	351.4 ± 2.3
Q	1997 Aug 27	0.2871 ± 0.0063	622 ± 14	122.5 ± 1.1
J'	1997 Nov 11	0.2628 ± 0.0049	630 ± 12	80.6 ± 1.1
[G'']	1998 Feb 19	0.2109 ± 0.0071	673 ± 23	3.7 ± 2.6
K	1997 Aug 27	0.3114 ± 0.0029	675 ± 6	204.7 ± 0.5
P	1997 Aug 27	0.3233 ± 0.0051	701 ± 11	73.4 ± 0.7
(S)	1997 Aug 27	0.3295 ± 0.0180	714 ± 39	54.9 ± 3.4
(N')	1997 Nov 11	0.3022 ± 0.0128	724 ± 31	253.1 ± 2.6
F'	1997 Nov 11	0.3107 ± 0.0085	745 ± 20	98.7 ± 1.6
L'	1997 Nov 11	0.3120 ± 0.0058	748 ± 14	356.1 ± 1.1
M	1997 Aug 27	0.3455 ± 0.0038	749 ± 8	186.6 ± 0.7
F	1997 Aug 27	0.3515 ± 0.0029	762 ± 6	91.9 ± 0.4
G	1997 Aug 27	0.3644 ± 0.0053	790 ± 12	108.3 ± 0.8
F''	1998 Feb 19	0.2961 ± 0.0043	944 ± 14	13.5 ± 0.7
[J'']	1998 Feb 19	0.3731 ± 0.0093	1190 ± 30	8.7 ± 1.3
(L'')	1998 Feb 19	0.4653 ± 0.0288	1484 ± 92	20.6 ± 1.8
(K'')	1998 Feb 19	0.5240 ± 0.0097	1671 ± 31	55.4 ± 1.2

Note.

^a The existence of the bracketed objects is somewhat uncertain ($3 < S/N < 4$), while the existence of the parenthesized objects is questionable and their detection marginal ($1.8 \leq S/N \leq 3$).

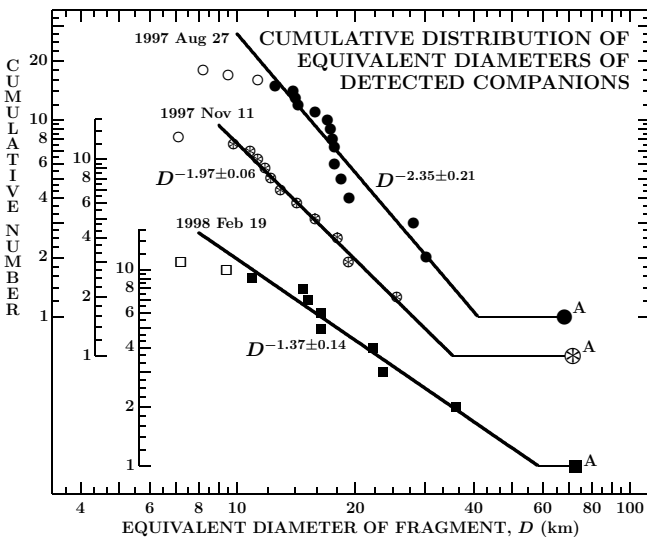


Figure 3. Cumulative distribution of equivalent diameters of the detected companions in the STIS images. The primary nucleus (A) and the companions of questionable existence (signal-to-noise ratio of ≤ 3 in Tables 6–8), shown by open symbols on the left, deviate from the distribution and were not employed in the fitting. The slope of the distribution drops rapidly with time.

Figure 3 displays the cumulative distribution of the detected companions' equivalent diameters, which measure, as in the instance of the primary nucleus, their observed cross-sectional areas. A striking property of the distribution is a very rapid rate of slope flattening with time, from $D^{-2.35 \pm 0.21}$ in August 1997 to $D^{-1.97 \pm 0.06}$ in November 1997, to $D^{-1.37 \pm 0.14}$ in February 1998. As the expected slope of a steady-state distribution law for fragments of a common parent is $D^{-2.5}$, described by Equation (12), the trend in the slope in Figure 3 points to a peculiar behavior, to be addressed below. Furthermore, the equivalent diameters of most companions are so large that they cannot be single fragments; instead, they appear to consist of subclusters of fragments.

The data points in Figure 3 that significantly deviate from the fitted power laws include the companions whose existence is questionable; this is understandable, because their signals barely exceeded the background signal of the extended source. Not only was their detection marginal, but there may have existed additional companions of similar equivalent diameters that failed to be detected at all, an argument that is in agreement with the positions of the doubtful companions consistently below the fitted laws in the figure. Alternatively, of course, there may not be any companions comparable in size or smaller than the questionable ones and the population of companions may terminate right there. Also deviating substantially from the fitted laws is the primary nucleus, especially in the first two of the STIS images; fairly large offsets are not unusual at the lower end of the cumulative distributions of statistical sets and are not necessarily worrisome.

As for the rapidly dropping slope of the cumulative distribution of the companions in Figure 3, I test an assumption that it is caused by temporal variations in the objects' cross-sectional area (measured by their equivalent diameter). The issue is important because if the companions are compact subclusters of fragments, their total cross sections may either increase with time as a result of progressive fragmentation because of collisions at very low velocities — or decrease also as a result of the fragmentation that entails escape of much of the involved mass from the gravity field of the subcluster once the debris acquired velocities that exceeded the escape limit. Which of the two processes dominates is determined by the systematic variations in the distribution's slope, linked to the cross-sectional variations with time.

I now examine under what set of circumstances could the steady-state cumulative distribution of companions, given by Equations (13), change dramatically its slope to fit the distributions in Figure 3. Let at time t_0 , when the process affecting the distribution of companions was set off, an equivalent diameter of the primary nucleus be $D_0^* = D_0^*(t_0)$, while a companion's equivalent diameter be $D^* = D^*(t_0) = D_1^*(t_0), D_2^*(t_0), \dots$ [$D^*(t_0) < D_0^*(t_0)$]. Calling $x = x(t_0) = D^*(t_0)/D_0^*(t_0)$, the steady-state cumulative distribution, \mathcal{N}_{nuc} , of the companion nuclei at time t_0 is, following Equation (13),

$$\mathcal{N}_{\text{nuc}}(t_0) = x^{-\kappa_0}, \quad (60)$$

where $x \leq 1$, $\kappa_0 = \frac{5}{2}$, $\mathcal{N}_{\text{nuc}} = 1$ for $x = 1$ (when $D^* = D_0^*$), and $\mathcal{N}_{\text{nuc}} > 1$ for $x < 1$.

At a time $t > t_0$, a different relationship applies, as is demonstrated by Figure 3. In particular, one now has $D_0^* = D_0^*(t)$, $D^* = D_1^*(t)$, $D_2^*(t), \dots$ [with $D_0^*(t) \neq D_0^*(t_0)$, $D_i^*(t) \neq D_i^*(t_0)$, $i = 1, 2, \dots$], $x = x(t) = D^*(t)/D_0^*(t)$, and, generally, $x(t) \neq x(t_0)$ with the exception of $x = 1$. The cumulative distribution at time t is described by

$$\mathcal{N}_{\text{nuc}}(t) = x^{-\kappa}, \quad (61)$$

where $\kappa \neq \kappa_0$ and constraints similar to those in Equation (60) apply to \mathcal{N}_{nuc} .

The issue now is to modify Equation (60) in a way such that it describes the cumulative distribution of equivalent diameters observed at time t and simultaneously reproduces the distribution in Equation (61). I search for a solution by adding a function $y(x)$, to be determined, to the variable x from Equation (61), so that Equation (60)

appears at time t as follows:

$$\mathcal{N}_{\text{nuc}}(t) = (x+y)^{-\kappa_0}. \quad (62)$$

The function y is subject to a boundary condition $y = 0$ at $x = 1$ in order that $\mathcal{N}_{\text{nuc}} = 1$. The log-log derivative of the expression (62) becomes

$$\frac{d \log \mathcal{N}_{\text{nuc}}}{d \log x} = \frac{x}{\mathcal{N}_{\text{nuc}}} \frac{d \mathcal{N}_{\text{nuc}}}{dx} = -\kappa_0 \frac{x}{x+y} \left(1 + \frac{dy}{dx} \right), \quad (63)$$

while from Equation (61) one gets immediately

$$\frac{d \log \mathcal{N}_{\text{nuc}}}{d \log x} = -\kappa. \quad (64)$$

Comparing the right-hand sides of the expressions (63) and (64), one obtains a linear differential equation of the first order,

$$\frac{dy}{dx} - \chi \frac{y}{x} = \chi - 1, \quad (65)$$

where $\chi = \kappa/\kappa_0 < 1$ because $\kappa < \kappa_0$ from Figure 3. The general solution to Equation (65) is

$$y(x) = c_0 x^\chi - x, \quad (66)$$

where c_0 is a constant; from the boundary condition for y in Equation (62) one finds $c_0 = 1$, so that

$$y(x) = x(x^{\chi-1} - 1). \quad (67)$$

Inserting from the solution (67) for y into Equation (62), one indeed obtains at once Equation (61). Since $\chi < 1$, y is positive for any $x < 1$ and, in conformity with Figure 3, the expression (67) implies that $x(t) < x(t_0)$ for any $\mathcal{N}_{\text{nuc}} > 1$; the process of accelerating escape of fragments from the companion clusters, entailing a progressively increasing loss of their cross-sectional area, dominates.

The observed slopes from Figure 3 can be fitted as a function of heliocentric distance r , expressed in units of perihelion distance q , by an exponential law of the type

$$\kappa(r) = \kappa_0 \exp \left\{ C_1 \left[1 - \left(\frac{r}{q} \right)^{C_2} \right] \right\}, \quad (68)$$

where C_1 and C_2 are constants. A fairly broad range of the pairs C_1, C_2 fits the slopes of the three observed distributions from Figure 3 about equally well, with the resulting residuals much smaller than the errors involved.

Table 10 presents the calculated values of the slopes κ and their residuals from one particular fit that employs $C_1 = +0.0024$ and $C_2 = +3.5$. Note that for $r = q$, Equations

Table 10
Fitting Slopes of Cumulative Distributions of Companion Nuclei in HST's STIS Images ($C_1 = 0.0024$, $C_2 = 3.5$)

Date of Observation	Distance to Sun		Distribution's Slope, κ			Ratio of Slopes, ^b $\chi = \kappa/\kappa_0$
	r (AU)	r/q	Observed ^a	Calc.	$O - C$	
1997 Aug 27	2.477	2.710	2.35 ± 0.21	2.317	+0.033	0.94 ± 0.08
1997 Nov 11	3.376	3.693	1.97 ± 0.05	1.987	-0.017	0.79 ± 0.02
1998 Feb 19	4.443	4.860	1.37 ± 0.14	1.365	+0.005	0.55 ± 0.06

Note.

^a From Figure 3.

^b Here $\kappa_0 = 2.5$ is the distribution's slope at steady state.

tion (68) always satisfies a condition $\kappa = \kappa_0 = 2.5$ regardless of the choice for C_1 and C_2 . It thus appears that the gradual loss of the cross-sectional area of the detected companions may have been triggered off by the Sun's significant near-perihelion perturbations of the motions of fragments in each companion's cluster, with some of them presumably lost to space at an accelerated rate after perihelion. The time of birth of the companions is unknown but the results suggest that the distribution of these subclusters of fragments still conformed to steady state at the time of perihelion passage.

If correct, this argument implies that the *preperihelion* distribution of equivalent diameters of companions was essentially in steady state. To test this inference, I examined the distribution for the image of 1996 October 17, in which 11 companions were detected, a greater number than in any other preperihelion image. I found that, once again, with the exception of the primary nucleus and a few companions of questionable existence at the other end of the distribution, the equivalent diameters of the remaining 8 companions fitted a power law with a slope of $\kappa = 2.67 \pm 0.22$, consistent within errors with the steady-state slope of 2.5.

A general picture of the distribution of equivalent diameters of the companions that emerges from these considerations is a possible cyclic variation in the slope: the assemblage of companions approaches perihelion with a steady-state distribution, but departs it with a distribution that is increasingly flatter. To retain this cycle from one revolution about the Sun to the next, the process of slope flattening is required to terminate at some time after perihelion and steady state to be gradually restored. It is probable that far from the Sun it is the collisions of fragments in the cluster of each companion (as well as the primary nucleus) that in the absence of the Sun's perturbations gradually re-establish steady state within the primary's cluster and, by extension, in the distribution of the companions' equivalent diameters as well. If so, the rapidly diminishing tilt of the distribution in an early post-perihelion span of time is merely a short-lived solar-perturbation effect.

Alternatively, the rapidly flattening slope of the distribution of the companions' equivalent diameters could represent a lasting effect that wiped out the steady-state distribution once and for all. If this interpretation is correct, it would imply the birth of the detected companions to date back to a time (or times) *after* the previous perihelion in the year of -2250 , as the steady-state distribution should otherwise have been done away with shortly after that time.

In either scenario, the practical issue is the degree of contamination caused by the companions in the primary nucleus' signal detected in the images taken at very large heliocentric distances after perihelion that Szabó et al. (2012) used in their investigation. For example, within a projected distance of 500 km of the primary nucleus, the companions contributed 71% of the primary nucleus' signal in the 1997 August image (Table 6), 40% in the 1997 November image (Table 7), and 39% in the 1998 February image (Table 8). If this trend continued, the contribution became probably close to negligible in an HST image of 2009 September 8, one of the images employed by Szabó et al. However, since the degree of contamination depends on the instrumental constants, it may

represent one of possible explanations for a minor gap of 0.19 mag between the 2009 HST observation and the 2011 October 23 VLT observations, which Szabó et al. attributed to an albedo difference.

In closing, a correlation is noticed in this context that appears to exist after perihelion between the decreasing slope of the distribution curve of the companions' equivalent diameters and the presence of the striking flare-ups on the comet's inner-coma light curve, observed by Liller (2001) (Section 9). Either phenomenon is proposed to be a signature of fragment collisions, in both the primary nucleus' cluster and the subclusters of the companions.

11.5. *Final Comments on the Problem of Companion Nuclei in C/1995 O1*

The first comment concerns the terminology. In my earlier paper (Sekanina 1999b) I consistently referred to a *satellite* or *satellites*, whereas now I am dealing with a *companion* or *companions*. As remarked at the beginning of Section 11, this change of terminology is a corollary of the new model for the comet's nucleus that implies a substantially lower mass of the cluster that makes up the primary nucleus, by a factor of more than 100, relative to the mass estimated for a solid nucleus of the same cross-sectional area. This difference clearly has an effect on the dimensions of the stability zone, with the result that the range of distances for gravitationally bound companions — the satellites — is now curtailed significantly.

The second comment is to underscore a point that appears to have never been contemplated in the controversy of the detection of a companion (or companions) in close proximity of the primary nucleus: the unequal degrees of fitness and resolution offered by the various applied techniques toward achieving a detection. I argue that a two-dimensional modeling of the type that the method employed here is based on is more robust and less prone to missing inconspicuous objects in close proximity of a major object than is, for example, the method of radial cuts used in Lamy's approach (e.g., Lamy et al. 1996).

The superior qualities of the applied technique are apparent not only from the high signal-to-noise ratios of the detected companions (as listed in Tables 6–8), but also from the results of experimentation with fitting additional extended sources to account for a complex distribution of the signal over the investigated field of view. Solutions with more than one extended source were not successful in fitting the local signal peaks, unlike the solutions with additional point sources. Thus, the present results cast doubts on the detected bumps in the digital maps as imprints of complex morphological features of the ambient dust coma (such as jets or hoods) and, instead, support the notion that they are signatures of point-like companion nuclei immersed in the coma.

12. SUMMARY AND CONCLUSIONS

A consensus is that C/1995 O1 was one of the most spectacular comets of the 20th century with an unusually large nucleus. However, even the best determination — based on the far-infrared observations with the Herschel Space Observatory when the comet was no longer active — entailed assumptions by employing a model that converted the observed flux, that is, a measure of the *cross-sectional area*, of 4300 km², to what should be called an equivalent diameter of 74 ± 6 km (Szabó et al. 2012).

Accordingly, it is the cross-sectional area — a quantity more directly measured than the diameter — that describes the nucleus more faithfully. It is then a matter of interpretation to decide what kind of nucleus the measured quantity characterizes, whether a single spherical solid body, or a binary object, or a cluster of solid spherical bodies of the same overall cross sectional area, etc. Subject to additional constraints, they all satisfy the flux condition equally well.

It is noted that Szabó et al.’s result is in excellent agreement with a mean equivalent diameter of 73.1 ± 2.4 km (Table 5), derived from the HST images taken on nine dates between 1995 October and 1998 February, when the comet was always less than 6.4 AU, and as close as 2.7 AU, from the Sun. This correspondence suggests that the comet’s dust coma was at these heliocentric distances optically thin all the way to the surface of the nucleus.

A gigantic size of the nucleus is fundamentally at odds with the independent detection of a fairly high outgassing-driven nongravitational acceleration that the comet’s orbital motion was subjected to (Paper 1). The acceleration, $(0.707 \pm 0.039) \times 10^{-8} \text{ AU day}^{-2}$ at a heliocentric distance of 1 AU and equal to $(2.39 \pm 0.13) \times 10^{-5}$ the Sun’s gravitational acceleration, follows a modified Marsden-Sekanina-Yeomans (1973) law with a scaling distance of $r_0 = 15.36$ AU. When integrated over the entire orbit about the Sun, the nongravitational effect is found to be equivalent to a momentum change per unit mass of $2.46 \pm 0.14 \text{ m s}^{-1}$. Accounting for the momentum exerted by the mass sublimated from the nucleus over the orbit, the conservation-of-momentum law suggests that such a nucleus of a bulk density of 0.4 g cm^{-3} should not exceed ~ 10 km in diameter and its mass should be on the order of 10^{17} g , more than *two orders of magnitude* less than the mass of the nucleus with the dimensions determined by Szabó et al. (2012).

I argue that this major conflict can only be avoided by postulating that the nucleus of C/1995 O1 at its recent return to perihelion was made up of a *compact cluster of massive fragments* of the original nucleus that broke up by the action of tidal forces exerted by Jupiter during the comet’s close encounter with the planet in the 23rd century BCE (Paper 1). Dominated by collisions, the cluster is assumed to have a size distribution of fragments that reached steady state, with their cumulative number varying inversely as a $\frac{5}{2}$ th power of fragment diameter. The nongravitational acceleration detected in the comet’s orbital motion is in this scenario interpreted as referring to the principal, most massive fragment, located near the cluster’s center of mass and, as required by the conservation-of-momentum law, up to 10 km in diameter. The nongravitational accelerations on other outgassing fragments remain undetected, triggering perturbations of their motions relative to the principal fragment.

Besides having a correct cross-sectional area, the cluster ought to appear as a nearly point-like feature in the high-resolution images taken with the HST instruments. This requisite limits the models to a strongly compacted cluster not exceeding ~ 200 km in diameter, constraining its image’s extent to no more than two pixels across on the HST detectors at geocentric distances of ~ 3 AU. Independently, the steady-state size distribution of fragments restricts the total mass of the cluster to less than five times the mass of the principal fragment.

Further critical properties of C/1995 O1 are the tensile strength of its original, pre-encounter nucleus as well as a degree of gravitational stability and collisional rate of the cluster-like nucleus. The mass of the pre-encounter nucleus is estimated at about 20 masses of the principal fragment and more than 20 km in diameter, with most of the mass having been lost by the time the comet was discovered in 1995. Given the minimum encounter distance of less than 11 Jovian radii (Paper 1), a critical tensile strength along fissures could not be higher than several Pa for the nucleus to fracture, while the central gravitational pressure did not exceed ~ 3000 Pa.

Based on existing studies of gravitational stability of globular clusters on the one hand and binary asteroids on the other hand, I adopt for the radius of a stability zone a conservative limit equaling $\sim \frac{1}{7}$ th the radius of the Hill sphere. For a cluster of fragments of the considered mass, the sphere of gravitational stability at perihelion of C/1995 O1 is slightly smaller than the cluster’s dimensions. Accordingly, significant perturbations of the cluster’s outer reaches by the Sun are likely near perihelion, resulting presumably in a higher collisional rate after perihelion, at least over limited periods of time.

Possible evidence for this corollary of the Sun’s near-perihelion perturbations is Liller’s (2001) list of recurring flare-ups in the comet’s inner coma, five of which were detected between early 1998 and mid-1999. An additional flare-up of similar nature was observed by other astronomers in late 1999, when Liller’s monitoring was incomplete. Interpreting the flare-ups as due to dust ejecta from colliding kilometer-sized fragments, Liller’s result provides their collisional rate, allowing thus to correlate the cluster’s dimensions with the principal fragment’s size and to select a narrow range of cluster models centered on the most probable one, presented in Table 11. The high chance of collisions among fragments is illustrated by an average distance between their centers, which is shorter than the diameters of the ~ 50 most massive fragments.

The proposed cluster model for the nucleus of comet C/1995 O1 so dramatically contrasts with the traditional single-body model that the published interpretations of the comet’s coma morphology and brightness variations have now become largely invalidated and will have to be reinvestigated essentially from scratch, an effort that is beyond the scope of this study. However, the flare-ups in the post-perihelion light curve of the inner coma (Liller 2001) are unlikely to be products of sudden local activity on a single rotating nucleus because identical areas of the surface would have been exposed to the Sun before perihelion, yet no flare-ups were detected along the incoming branch of the orbit.

Also beyond this investigation’s scope is a highly desirable Monte Carlo-type modeling of the fragments’ motions in the nucleus cluster over long periods of time, involving an n-body problem. This task should be undertaken to assess the degree of the cluster’s gravitational stability along the preperihelion leg of the orbit, the severity of the Sun’s perturbations especially around perihelion given that the size of the stability zone is then found to be slightly smaller than the cluster’s size, and the magnitude of their effects on the motions of individual fragments inside or outside the cluster along the post-perihelion leg of the orbit.

Table 11Adopted Model Parameters for Compact-Cluster Nucleus of C/1995 O1 (assumed bulk density 0.4 g cm^{-3})

Model Parameter	Value
Cluster of Fragments at 1997 Apparition	
Diameter of principal fragment, D_0 (km)	8.5
Mass of principal fragment, \mathcal{M}_0 (10^{17} g)	1.3
Diameter of smallest fragment, D_* (m)	32.6
Mean diameter of fragments, $\langle D \rangle$ (m)	54.3
Total number of fragments in cluster, $\mathcal{N}_{\text{frg}}^*$ (10^6)	1.1
Total mass of fragments, \mathcal{M}_{frg} (10^{17} g)	6.0
Diameter of stability zone at perihelion, $D_{\text{st}}(q)$ (km)	183
Breakup of Original Nucleus at Jovian Encounter Time	
Diameter, D_C (km)	23
Mass, \mathcal{M}_C (10^{17} g)	26
Central gravitational pressure, P_C (10^3 Pa)	3.0
Tensile strength (upper limit), T_{tens} (Pa)	4.2
Collisional Process in Cluster at 1997 Apparition	
Cluster's collisional diameter, D_{frg} (km)	207
Average number density of fragments, ν (km^{-3})	0.24
Average optical depth, Θ	0.14
Average distance between centers of fragments, s_{frg} (km)	1.8
Mean collisional cross-sectional area of fragments (all events), $\langle \sigma \rangle$ (km^2)	0.012
Mean quadratic collisional relative (or impact) velocity of fragments, $\langle V_{\text{rel}}^2 \rangle^{1/2}$ (m s^{-1})	0.48
Velocity of escape at distance $\frac{1}{2}D_{\text{frg}}$ from center of cluster, V_{esc} (m s^{-1})	0.88
Mean collisional rate (all events), $1/\tau_{\text{coll}}$ (days^{-1})	0.12
Mean collisional rate (Liller-type events, $D \geq 1.2$ km), $(1/\tau_{\text{coll}})_{\text{obs}}$ (yr^{-1})	3.2

A final comment on the compact-cluster model of the nucleus of C/1995 O1 relates to a major imbalance between the masses of the original, pre-encounter nucleus and the cluster structure at the 1997 apparition, by which time the comet is estimated to have lost about three quarters of its initial mass, most of it in direct orbits apparently soon after the encounter. It is expected that attrition was also likely to accompany the process of perturbing the motions of fragments near the 1997 perihelion. Given the submeter-per-second velocities of fragments, this scenario invites a suggestion that a fraction of the perturbed fragments or subclusters of fragments escaped the main cluster's gravity shortly following the perihelion passage and that such boulder-sized debris should be scattered near the comet and might show up in the HST's post-perihelion images from 1997 August 27 through 1998 February 19. Indeed, a fragment moving with a velocity of escape radially away from the primary nucleus' cluster in free flight would be expected to reach a distance of ~ 1000 km from it in a matter of a few weeks; in reality, the time needed to reach this distance would be longer by a factor of a few. And closer objects may represent stray fragments or subclusters of fragments whose relative velocities were just below the velocity of escape. Inspection of the immediate proximity of the primary nucleus for such stray objects was therefore eminently desirable and a computer search harvested more than 30 objects in the three post-perihelion HST images and at least 15 in the first of them alone.

The detected signals of these companions suggest that they in fact are subclusters of fragments because, if single objects, most of them would be larger than the principal fragment of the primary nucleus' cluster. Their signal-to-noise ratios are generally quite high, and the possibility that they all are factitious products of the search algorithm is so remote that it can safely be dismissed. Also, there is no correlation between their locations and the positions and directions of bright jet-like features in the images. As to the old controversy on the detection of a companion (or satellite) in the HST images, it could very well be that it is the applied computer technique's faculty, aptitude, and sensitivity to extracting the object's signal that makes the difference, a point never raised in the past.

While the times of the post-perihelion HST images were judged to be separated by gaps too wide to establish identities of the companions in different images, the data set was considered appropriate for investigating the cumulative distribution of their signals (or equivalent diameters) separately in each frame. The result was a surprisingly rapid systematic drop in the slope of the distribution from a rate lower than, but fairly close to, the steady-state rate in the 1997 August 27 image to a rate about 1.7 times less steep in the 1998 February 19 image. The trend is explained as an effect of a gradual dissipation of the subclusters that make up the companions, whereby the more massive subclusters decay at a slower pace than the less massive ones. Quantitative analysis implies that when extrapolated back in time, the steady-state distribution would have been reached near perihelion, a coincidence that suggests a possible relationship between the separation of the subclusters from the primary and the Sun's peak perturbations.

I do realize that the developed compact-cluster model, while self-consistent, might be deemed by some as controversial and certainly in need of further testing. Similarly, some of the comet's properties might be hard to make readily compatible with this model or they might require additional constraints or introduce further conditions. Whatever difficulties might lie ahead, however, the major disparity between the outgassing-driven nongravitational acceleration — which for C/1995 O1 exceeds, or is comparable to, nongravitational accelerations derived in the past for fairly bright, but by no means spectacular, long-period comets⁹ — and the single-body model, which for C/1995 O1 requires a nucleus 74 km in diameter and nearly 10^{20} g in mass, strikes one as so utterly compelling that to me this argument alone rules the traditional, single-body model out completely. And I am aware of no other model that would stand.

I thank Franck Marchis for providing me with the digital maps of the three post-perihelion HST images made with the STIS instrument in 1997–1998. This research was carried out at the Jet Propulsion Laboratory, California Institute of Technology, under contract with the National Aeronautics and Space Administration.

⁹ For example, for comet C/1998 T1 the total nongravitational parameter amounted to $0.88 \times 10^{-8} \text{ AU day}^{-2}$ (Nakano 2000); for C/2000 WM₁ to $0.52 \times 10^{-8} \text{ AU day}^{-2}$ (Nakano 2002); and for the main component B of C/2001 A2 to $0.59 \times 10^{-8} \text{ AU day}^{-2}$ (Nakano 2001). (The errors are in the second or higher decimal.)

REFERENCES

- Aggarwal, H. R., & Oberbeck, V. R. 1974, *ApJ*, 191, 577
- Basilevsky, A. T., Krasil'nikov, S. S., Shirayev, A. A., et al. 2016, *Solar Sys. Res.*, 50, 225
- Baum, S. 1996, *STIS Instrument Handbook, Version 1.0.* (Baltimore: Space Telescope Science Institute)
- Bessel, F. W. 1836, *AN*, 13, 185
- Biver, N., Bockelée-Morvan, D., Crovisier, J., et al. 2002, *Earth Moon Plan.*, 90, 5
- Brownlee, D. E. 1985, *Annu. Rev. Earth Plan. Sci.*, 13, 147
- Chebotaev, G. A. 1964, *Sov. Astron.*, 7, 618
- Crovisier, J., Bockelée-Morvan, D., Colom, P., et al. 2004, *A&A*, 418, 1141
- Della Corte, V., Rotundi, A., Fulle, M., et al. 2015, *A&A*, 583, A13
- Dohnanyi, J. S. 1969, *JGR*, 74, 2531
- Fernández, Y. R. 2002, *Earth Moon Plan.*, 89, 3
- Fernández, Y. R., Wellnitz, D. D., Buie, M. W., et al. 1999, *Icarus*, 140, 205
- Fulle, M., Cremonese, G., & Böhm, C. 1998, *AJ*, 116, 1470
- Griffin, I. P., & Bos, M. 1999, *IAUC 7288*
- Groussin, O., Jorda, L., Auger, A.-T., et al. 2015, *A&A* 583, A32
- Gunkelmann, N., Ringl, C., & Urbassek, H. M. 2016, *A&A*, 589, A30
- Hamilton, D. P., & Burns, J. A. 1991, *Icarus*, 92, 118
- Hamilton, D. P., & Burns, J. A. 1992, *Icarus*, 96, 43
- Jorda, L., Lamy, P., Groussin, O., et al. 2000, in *ISO Beyond Point Sources: Studies of Extended Infrared Emission*, ESA-SP 455, ed. R. J. Laureijs, K. Leech, & M. F. Kessler (Noordwijk, Netherlands: ESTEC), 61
- Kennedy, G. F. 2014, *MNRAS*, 444, 3328
- Kessler, D. J. 1981, *Icarus*, 48, 39
- Kramer, E. A., Fernández, Y. R., Lisse, C. M., et al. 2014, *Icarus*, 236, 136
- Lamy, P. L., Toth, I., Grün, E., et al. 1996, *Icarus*, 119, 370
- Lamy, P. L., Toth, I., Fernández, Y. R., & Weaver, H. A. 2004, in *Comets II*, ed. M. C. Festou, H. U. Keller, & H. A. Weaver (Tucson: University of Arizona Press), 223
- Licandro, J., Bellot Rubio, L. R., Boehnhardt, H., et al. 1998, *ApJ*, 501, L221
- Liller, W. 1997, *Plan. Space Sci.*, 45, 1505
- Liller, W. 2001, *Int. Comet Q.*, 23, 93
- Marchis, F., Boehnhardt, H., Hainaut, O. R., & Le Mignant, D. 1999, *A&A*, 349, 985
- Marcus, J. N. 2007, *Int. Comet Q.*, 29, 39
- Mardling, R. A. 2008, in *The Cambridge N-Body Lectures, Lecture Notes in Physics*, ed. S. J. Aarseth, C. A. Tout, & R. A. Mardling (Berlin: Springer), 760, 59
- Marsden, B. G. 1968, *AJ*, 73, 367
- Marsden, B. G. 1969, *AJ*, 74, 720
- Marsden, B. G., Sekanina, Z., & Yeomans, D. K. 1973, *AJ*, 78, 211
- McCarthy, D. W., Stolovy, S., Campins, H., et al. 2007, *Icarus*, 189, 184
- Merouane, S., Zaprudin, B., Stenzel, O., et al. 2016, *A&A*, 596, A87
- Nakano, S. 2000, *Minor Plan. Circ.* 40668
- Nakano, S. 2001, *Minor Plan. Circ.* 44030
- Nakano, S. 2002, *Minor Plan. Circ.* 46619
- Pearce, A. R. 1999, *IAUC 7288*
- Probstein, R. F. 1969, in *Problems of Hydrodynamics and Continuum Mechanics*, ed. F. Bisshopp & L. I. Sedov (Philadelphia: Soc. Ind. Appl. Math.), 568
- Rigaut, F., Salmon, D., Arsenault, R., et al. 1998, *PASP*, 110, 152
- Samarasinha, N. H. 2000, *ApJ*, 529, L107
- Schräpler, R., Blum, J., Seizinger, A., & Kley, W. 2012, *ApJ*, 758, 35
- Sekanina, Z. 1987, in *Diversity and Similarity of Comets*, ESA SP-278, ed. E. J. Rolfe & B. Battrick (Noordwijk, Netherlands: ESTEC), 315
- Sekanina, Z. 1995, *A&A*, 304, 296
- Sekanina, Z. 1998, *ApJ*, 509, L133
- Sekanina, Z. 1999a, *Earth Moon Plan.*, 77, 147
- Sekanina, Z. 1999b, *Earth Moon Plan.*, 77, 155
- Sekanina, Z., & Kracht, R. 2017, eprint arXiv:1703.00928 (Paper 1)
- Sosa, A., & Fernández, J. A. 2011, *MNRAS*, 416, 767
- Szabó, Gy. M., Sárneczky, K., & Kiss, L. L. 2011, *A&A*, 531, A11
- Szabó, Gy. M., Kiss, L. L., Pál, A., et al. 2012, *ApJ*, 761, 8
- Vasundhara, R., & Chakraborty, P. 1999, *Icarus*, 140, 221
- Weaver, H. A., & Lamy, P. L. 1999, *Earth Moon Plan.*, 79, 17
- Weaver, H. A., Feldman, P. D., A'Hearn, M. F., et al. 1999, *Icarus*, 141, 1
- Whipple, F. L. 1950, *ApJ*, 111, 375
- Williams, D. R., & Wetherill, G. W. 1994, *Icarus*, 107, 117